MOTOROLA LABS

COMPUTATIONAL EME COMPLIANCE ASSESSMENT OF THE XTL5000 VHF MOBILE RADIO, MODEL # M20KTS9PW1AN, FCC ID AZ492FT3808

July 19, 2004 – Revised October 4, 2004

Giorgi Bit-Babik and Antonio Faraone
Motorola Corporate EME Research Lab, Plantation, Florida

Introduction

This report summarizes the computational [numerical modeling] analysis performed to document compliance of the XTL5000 VHF, Model Number M20KTS9PW1AN, Mobile Radio and vehicle-mounted antennas with the Federal Communications Commission (FCC) guidelines for human exposure to radio frequency (RF) emissions. The radio operates in the 136 - 174 MHz frequency band.

This computational analysis supplements the measurements conducted to evaluate the FCC *maximum permissible exposure* (MPE) limits for this mobile device. All test conditions (26 in total) that did not conform with applicable MPE limits were subdivided into two groups — bystander exposures and passenger exposures — and analyzed to determine whether those conditions complied with the *specific absorption rate* (SAR) limits for general public exposure (1.6 W/kg averaged over 1 gram of tissue and 0.08 W/kg averaged over the whole body) set forth in FCC guidelines, which are based on the IEEE C95.1-1999 standard [1]. For both groups, a commercial code based on Finite-Difference-Time-Domain (FDTD) methodology was employed to carry out the computational analysis. It is well established and recognized within the scientific community that SAR is the primary dosimetric quantity used to evaluate the human body's absorption of RF energy and that MPEs are in fact derived from SAR. Accordingly, the SAR computations provide a scientifically valid and more accurate estimate of human exposure to RF energy.

Method

The simulation code employed is XFDTD™ v5.3, by Remcom Inc., State College, PA. This computational suite features a heterogeneous full body standing model (High Fidelity Body Mesh), derived from the so-called Visible Human [2], discretized in 5 mm voxels. The dielectric properties of 23 body tissues are automatically assigned by XFDTD™ at any specific frequency. The "seated" man model was obtained from the standing model by modifying the articulation angles at the hips and the knees. Details of the computational method and model are provided in the Appendix to this report, following the structure outlined in Appendix B.III of the Supplement C to the FCC OET Bulletin 65.

The car model has been imported into XFDTD™ from the CAD file of a sedan car having dimensions 4.98 m (L) x 1.85 m (W) x 1.18 m (H), and discretized in 5mm voxels. For trunk mounted antennas, the wheels and part of the hood were omitted in order to fit within the computational memory (3 GB) available. For roof mounted antennas, part of the trunk had to be removed while maintaining the integrity of the roof connection with the car body. These omissions would not be expected to affect the exposure calculations in any event.

For bystander exposure, the antenna position is 26 cm from the end of the trunk, so as to replicate the experimental conditions used in MPE measurements. For passenger exposure, the distance of trunk mounted antennas from the passenger head was set at 85 cm, so as to replicate the experimental conditions used in MPE measurements. Figures 1 shows one of the XFDTD™ computational models used for bystander exposure. Figures 2 and 3 show some of the XFDTD™ computational models used for passenger exposure to trunk and roof mounted antennas, respectively.

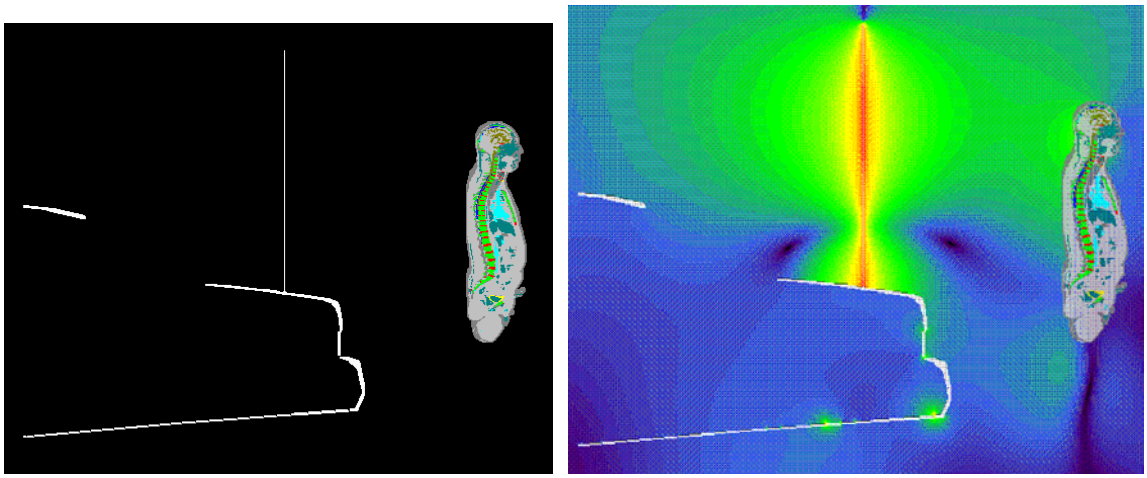

Figure 1: Bystander model exposed to a trunk-mount gain antenna (121.5 cm) operating at 155 MHz: XFDTD geometry and H-field distribution. The antenna is mounted in the center of the trunk.

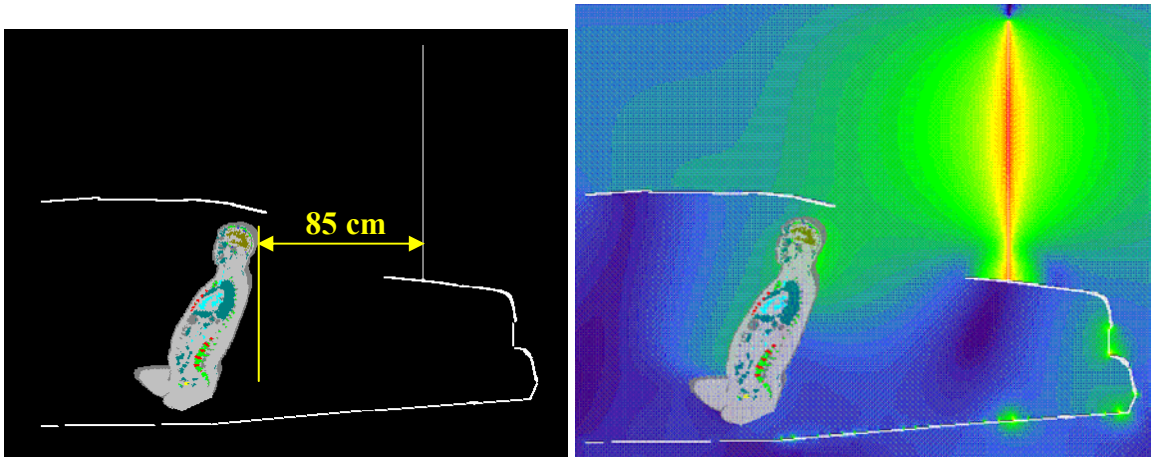

Figure 2: Passenger model exposed to a trunk-mount gain antenna (121.5 cm) operating at 155 MHz: XFDTD geometry and H-field distribution. The antenna is mounted at 85 cm from the passenger.

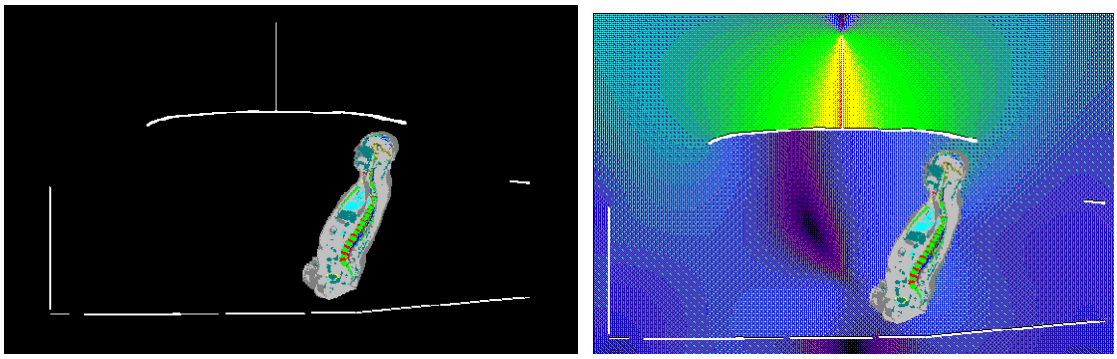

Figure 3: Passenger model exposed to a roof-mount quarter-wave antenna operating at 136 MHz: XFDTD geometry and H-field distribution. The antenna is mounted in the center of the roof.

The computational code employs a time-harmonic excitation to produce a steady state electromagnetic field in the exposed body. Subsequently, the corresponding SAR distribution is automatically processed in order to determine the whole-body and 1-g average SAR. The product maximum output power is 120 W rms. Since the ohmic losses in the cable and in the car materials, as well as the mismatch losses at the antenna feed-point, are neglected, and source-based time averaging (50% talk time) is employed, all computational results are normalized to half of it, i.e., 60 W *rms* net output power.

Results of SAR computations for bystanders

The test conditions requiring SAR computations are summarized in Tables I and II, together with other relevant information and the SAR results. With trunk mount antennas, the bystander is placed next to the trunk of the car, straight back, at 45 degrees from the longitudinal car centerline, and at 90 degrees from it, at a distance of 90 cm from the antenna while maintaining at least 20 cm from the vehicle body, so as to replicate the conditions used in MPE measurements. With roof mount antennas, the bystander is placed on the side of the car, facing or looking away from the antenna, at a distance of 90 cm from the antenna while maintaining at least 20 cm from the vehicle body. Twenty cases of bystander - facing towards to or away from the car - were simulated individually.

Table I: Results of the SAR computations for bystander exposure (50% talk-time) behind the car at a separation distance of 90 cm from the trunk-mount antenna while maintaining at least 20 cm from the vehicle body.

Antenna Kit #	Antenna length		Freq [MHz]	Bystander exposure	Exposure angle	SAR [W/kg]	
	Physical	XFDTD				1-g	WB
HAD4014A	116.8 cm	117 cm	155	Front	0 deg	1.14	0.018
HAD4014A	116.8 cm	117 cm	155	Back	0 deg	0.75	0.018
RAD4000A	118.5 cm	118.5 cm	155	Front	0 deg	1.08	0.017
RAD4000A	118.5 cm	118.5 cm	155	Back	0 deg	0.96	0.017
RAD4010ARB	121.4 cm	121.5 cm	155	Front	0 deg	1.00	0.016
RAD4010ARB	121.4 cm	121.5 cm	155	Back	0 deg	0.98	0.017
RAD4010ARB	121.4 cm	121.5 cm	155	Front	45 deg	0.94	0.017
RAD4010ARB	121.4 cm	121.5 cm	155	Back	45 deg	0.98	0.017
RAD4010ARB	121.4 cm	121.5 cm	155	Front	90 deg	0.73	0.015
RAD4010ARB	121.4 cm	121.5 cm	155	Back	90 deg	0.69	0.016

Table II: Results of the SAR computations for bystander exposure (50% talk-time) on the side of the car at a separation distance of 90 cm from the roof-mount antenna while maintaining at least 20 cm from the vehicle body.

Antenna Kit #	Antenna length		Freq [MHz]	Bystander exposure	SAR [W/kg]	
	Physical	XFDTD				
HAD4007A	49 cm	49 cm	146	Front	0.57	0.012
HAD4007A	49 cm	49 cm	146	Back	0.46	0.012
HAD4008A	45.6 cm	45.5 cm	155	Front	0.81	0.018
HAD4008A	45.6 cm	45.5 cm	155	Back	0.61	0.019
HAD4016A	50.5 cm	50.5 cm	136	Front	0.32	0.012
HAD4016A	50.5 cm	50.5 cm	136	Back	0.47	0.013
HAD4016A	50.5 cm	50.5 cm	149	Front	0.71	0.014
HAD4016A	50.5 cm	50.5 cm	149	Back	0.53	0.014
HAD4017A	47.5 cm	47.5 cm	146	Front	0.59	0.012
HAD4017A	47.5 cm	47.5 cm	146	Back	0.47	0.012

Limited to the cases of the trunk-mount antennas analyzed, the SAR distribution for the exposure condition (155 MHz, bystander at 0 degrees facing the car, trunk-mount HAD4014A antenna) that produced the highest peak 1-g and whole body SAR averages is shown in Fig. 4.

Limited to the cases of the roof-mount antennas analyzed, the SAR distribution for the exposure condition (155 MHz, bystander facing the car, HAD4008A antenna) that produced the highest peak 1-g SAR averages is shown in Fig. 5, while the condition that produced the highest whole body SAR averages is shown in Fig. 6 (155 MHz, bystander facing away from the car, HAD4008A antenna).

The overall maximum peak 1-g SAR is 1.14 W/kg, less than the 1.6 W/kg limit, while the maximum whole-body average SAR is 0.019 W/kg, less than the 0.08 W/kg limit.

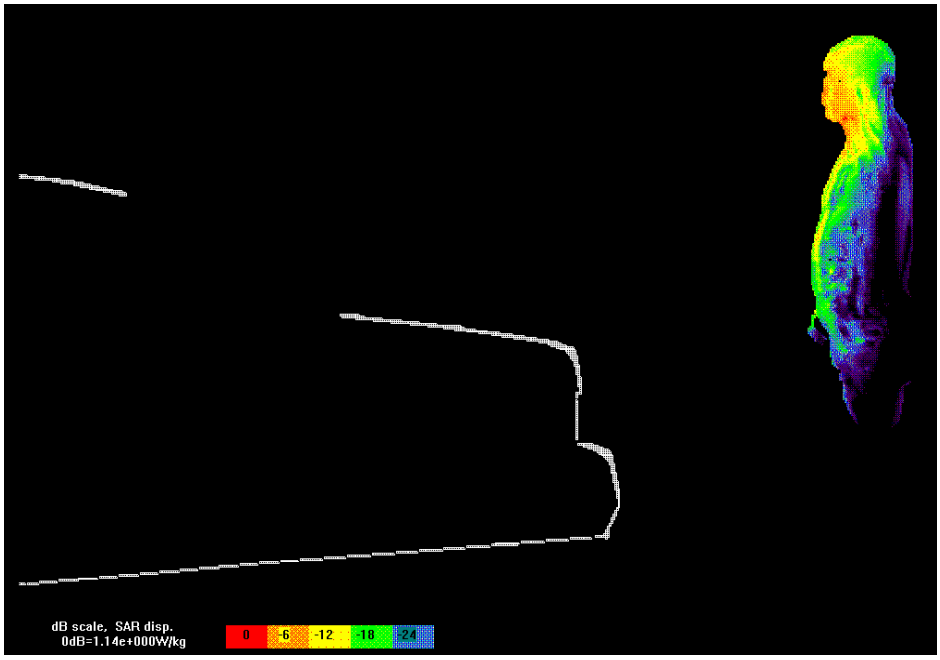

Figure 4. SAR distribution at 155 MHz for the bystander at 90 cm from the 117 cm gain antenna, placed in the center of the trunk, when facing the car at 0 degrees. The contour plot in the figure is relative to the plane where the peak 1-g average SAR for this exposure condition occurs.

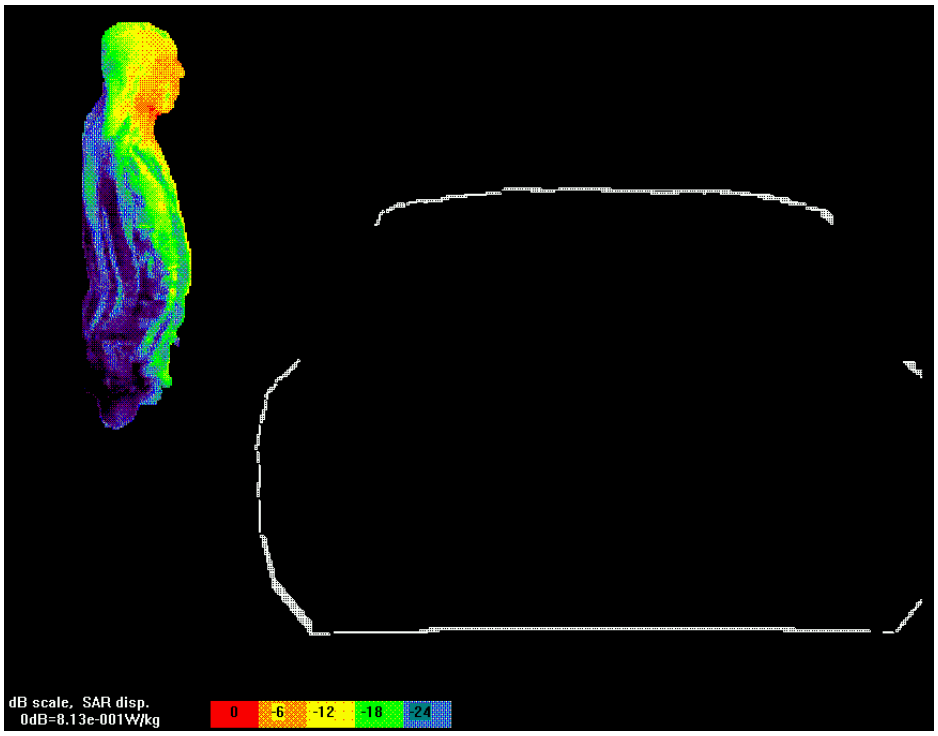

Figure 5. SAR distribution at 155 MHz for bystander at 20 cm from the side of the car (108 cm from the antenna), with the antenna at the roof center, when facing the car. The contour plot in the figure is relative to the plane where the peak 1-g average SAR for this exposure condition occurs.

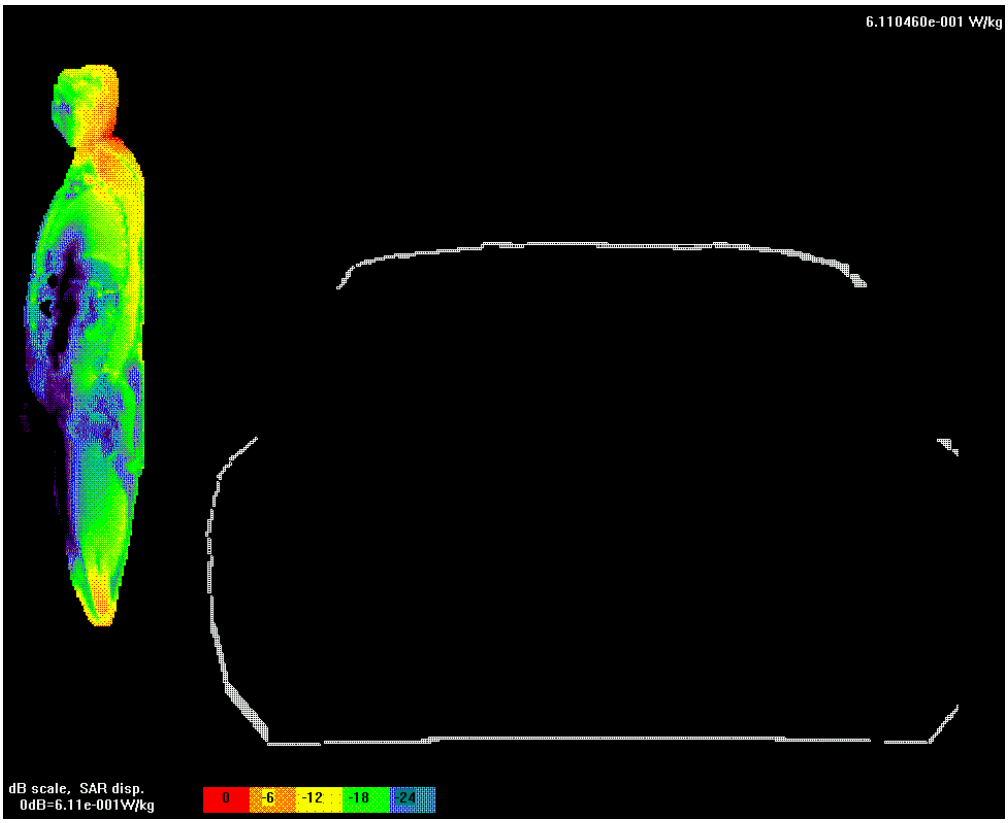

Figure 6. SAR distribution at 155 MHz for bystander at 20 cm from the side of the car (108 cm from the antenna), with the HAD4008A antenna at the roof center, when facing away from the car. The contour plot in the figure is relative to the plane where the peak 1-g average SAR for this exposure condition occurs.

Results of SAR computations for car passengers

The 18 test conditions requiring SAR computations are summarized in Table III, together with the antenna data and the SAR results. The conditions are for antenna mounted on the roof and on the trunk. The passenger is located in the center or on the side of the rear seat. The passenger model is surrounded by air, as the seat, which is made out of poorly conductive fabrics, is not included in the computational model. All the transmit frequency, antenna length, and passenger location combinations reported in Table II have been simulated individually. The maximum peak 1-g SAR is 0.50 W/kg, while the maximum whole-body average SAR is 0.018 W/kg.

Table III: Results of the SAR computations for passenger exposure (50% talk-time).

Mount location	Antenna Kit #	Antenna length		Freq [MHz]	Exposure location	SAR [W/kg]	
		Physical	XFDTD			1-g	WB
Roof	**HAD4006A**	52 cm	52 cm	136	center	0.17	0.010
Roof	**HAD4006A**	52 cm	52 cm	136	side	0.23	0.013
Roof	**HAD4007A**	49 cm	49 cm	146	center	0.50	0.015
Roof	**HAD4007A**	49 cm	49 cm	146	side	0.47	0.018
Roof	**HAD4008A**	45.6 cm	45.5 cm	155	center	0.30	0.008
Roof	**HAD4008A**	45.6 cm	45.5 cm	155	side	0.36	0.010
Roof	**HAD4016A**	50.5 cm	50.5 cm	162	center	0.18	0.006
Roof	**HAD4016A**	50.5 cm	50.5 cm	162	side	0.22	0.008
Roof	**HAD4016A**	50.5 cm	50.5 cm	136	center	0.20	0.011
Roof	**HAD4016A**	50.5 cm	50.5 cm	136	side	0.23	0.013
Roof	**HAD4016A**	50.5 cm	50.5 cm	149	center	0.49	0.013
Roof	**HAD4016A**	50.5 cm	50.5 cm	149	side	0.50	0.016
Roof	**HAD4017A**	47.5 cm	47.5 cm	160	center	0.22	0.006
Roof	**HAD4017A**	47.5 cm	47.5 cm	160	side	0.23	0.008
Roof	**HAD4017A**	47.5 cm	47.5 cm	146	center	0.48	0.014
Roof	**HAD4017A**	47.5 cm	47.5 cm	146	side	0.48	0.018
Trunk	**RAD4010ARB**	121.4 cm	121.5 cm	136	center	0.47	0.009
Trunk	**RAD4010ARB**	121.4 cm	121.5 cm	136	side	0.46	0.012

Limited to the cases of roof-mount antennas analyzed, the SAR distribution in the passenger model in the exposure condition that gave highest 1-g SAR is reported in Fig. 7 (146 MHz, passenger in the center of the back seat, HAD4007A antenna), while that for the exposure condition that gave highest whole-body average SAR is reported in Fig. 8 (146 MHz, passenger in the side of the back seat, HAD4017A antenna).

Finally, limited to the cases of the trunk-mount antennas analyzed, the SAR distribution in the passenger model in the exposure condition that gave highest 1-g SAR is reported in Fig. 9 (136 MHz, passenger in the center of the back seat, RAD4010ARB antenna), while that for the exposure condition that gave highest whole-body average SAR is reported in Fig. 10 (136 MHz, passenger in the side of the back seat, RAD4010ARB antenna).

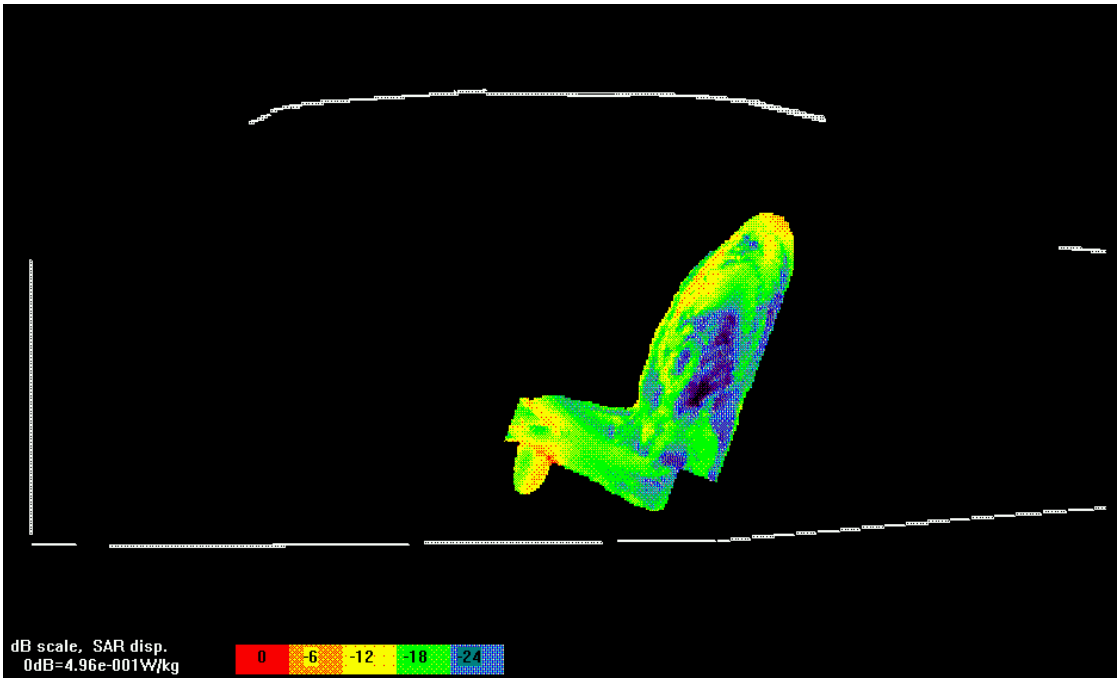

Figure 7. SAR distribution at 146 MHx in the passenger located in the center of the back seat, produced by the roof-mount HAD4007A antenna. The contour plot in the figure is relative to the plane where the peak 1-g average SAR for this exposure condition occurs.

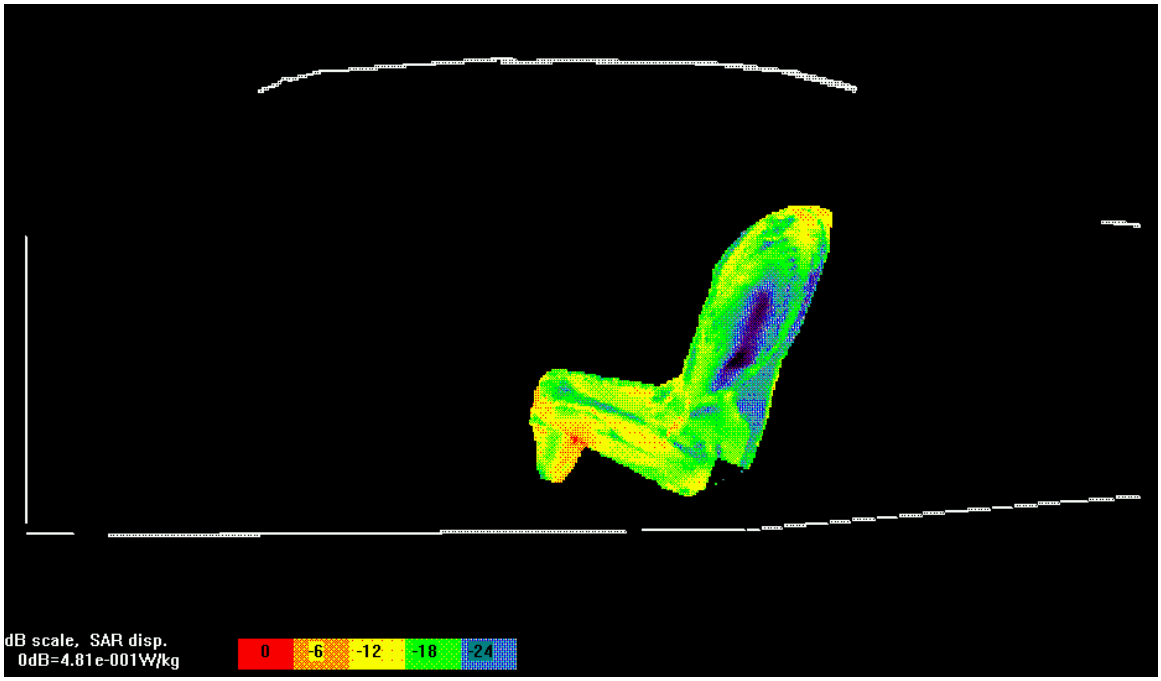

Figure 8. SAR distribution at 146 MHx in the passenger located in the side of the back seat, produced by the roof-mount HAD4017A antenna. The contour plot in the figure is relative to the plane where the peak 1-g average SAR for this exposure condition occurs.

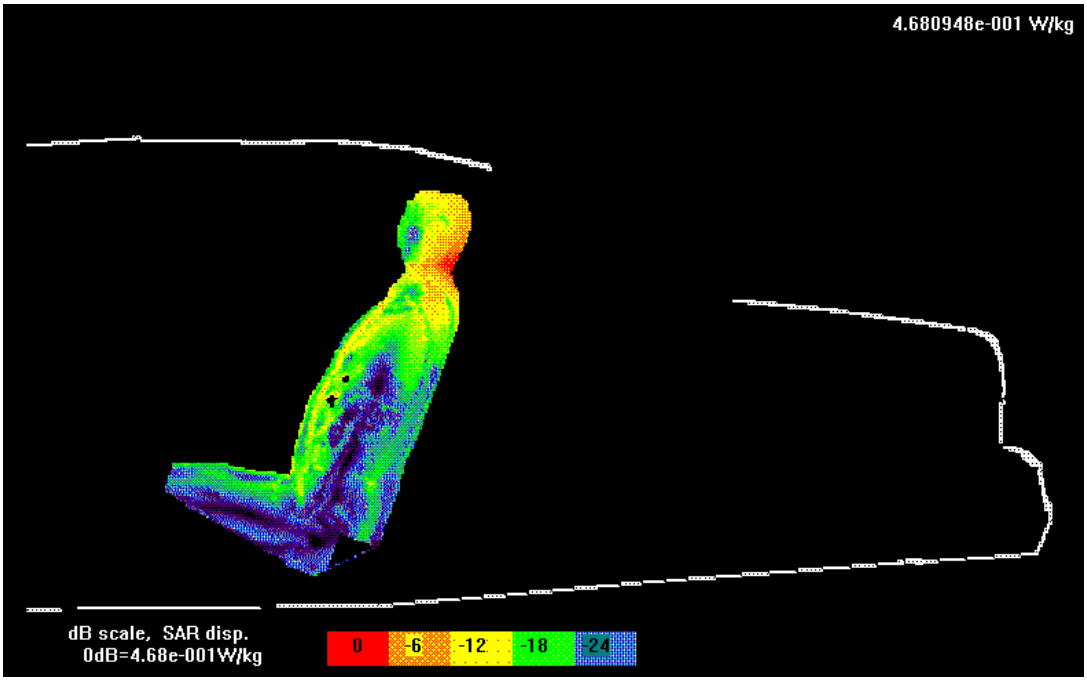

Figure 9. SAR distribution at 136 MHx in the passenger located in the center of the back seat, produced by the trunk-mount RAD4010ARB antenna. The contour plot in the figure is relative to the plane where the peak 1-g average SAR for this exposure condition occurs.

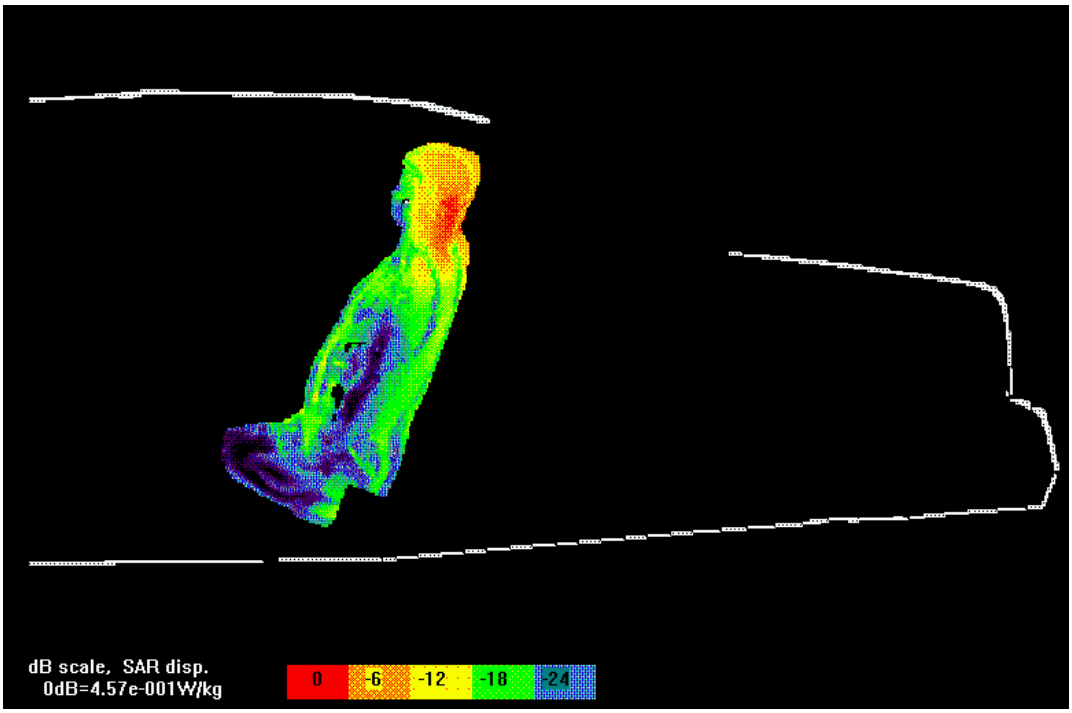

Figure 10. SAR distribution at 136 MHx in the passenger located in the side of the back seat, produced by the trunk-mount RAD4010ARB antenna. The contour plot in the figure is relative to the plane where the peak 1-g average SAR for this exposure condition occurs.

Conclusions

Under the test conditions described for evaluating passenger and bystander exposure to the RF electromagnetic fields emitted by vehicle-mounted antennas used in conjunction with this mobile radio product, the present analysis shows that the computed SAR values are compliant with the FCC exposure limits for the general public.

References

[1] IEEE Standard C95.1-1999. *IEEE Standard for Safety Levels with Respect to Human Exposure to RF Electromagnetic Fields*, 3 kHz to 300 GHz.

[2] http://www.nlm.nih.gov/research/visible/visible_human.html

APPENDIX: SPECIFIC INFORMATION FOR SAR COMPUTATIONS

This appendix follows the structure outlined in Appendix B.III of the Supplement C to the FCC OET Bulletin 65. Most of the information regarding the code employed to perform the numerical computations has been adapted from the XFDTD™ v5.3 User Manual. Remcom Inc., owner of XFDTD™, is kindly acknowledged for the help provided.

1) Computational resources

a) A four-processor server (Mod. PowerEdge 6650, by Dell Computers Inc.) equipped with four 1.4 GHz Xeon microprocessors and 4 GB D-RAM (3 GB available for running applications) was employed for all simulations.

b) The memory requirement was between 2 GB and 3 GB in all cases. Using the above-mentioned server with all four processors operating concurrently, the typical simulation would run for 22 hours.

2) FDTD algorithm implementation and validation

a) We employed a commercial code (XFDTD™ v5.3, by Remcom Inc.) that implements the classical Yee's FDTD formulation [1]. The solution domain was discretized according to a rectangular grid with a uniform 5 mm step in all directions. Sub-gridding was not used. Liao's absorbing boundary conditions [2] are set at the domain boundary to simulate free space radiation processes. The excitation is a lumped voltage generator with 50-ohm source impedance. The code allows selecting *wire objects* without specifying their radius. We used a wire to represent the antenna. The car body is modeled by solid metal. We did not employ the "thin wire" algorithm in XFDTD™ since the antenna radius was never smaller than one-fifth the voxel dimension. In fact, the XFDTD™ manual specifies that "Thin Wire materials may be used in special situations where a wire with a radius much smaller than the cell size is required… in cases where the wire radius is important to the calculation and is less than approximately 1/5 the cell size, the thin wire material may be used to accurately simulate the correct wire dimensions." The voxel size in all our simulations was 5 mm, and the antenna radius is always at least 1 mm (1 mm for the short quarter-wave antennas and 1.5 mm for the long gain antennas), so there was no need to specify a "thin wire" material. Because the field impinges on the bystander or passenger model at a distance of several tens of voxels from the antenna, the details of antenna wire modeling are not expected to have significant impact on the exposure level.

b) XFDTD™ is one of the most widely employed commercial codes for electromagnetic simulations. It has gone through extensive validation and has proven its accuracy over time in many different applications. One example is provided in [3].

We carried out a validation of the code algorithm by running the canonical test case involving a half-wave wire dipole. The dipole is 0.475 times the free space wavelength at

160 MHz, i.e., 88.5 cm long. The discretization used in the model was uniform in all directions and equal to 5 mm, so the dipole was 177 cells long. Also in this case, the "thin wire" model was not needed. The following picture shows XFDTD™ outputs regarding the antenna feed-point impedance (72.6 – j 11.8 ohm), as well as qualitative distributions of the total E and H fields near the dipole. The radiation pattern is shown as well (one lobe in elevation). As expected, the 3 dB beamwidth is about 78 degrees.

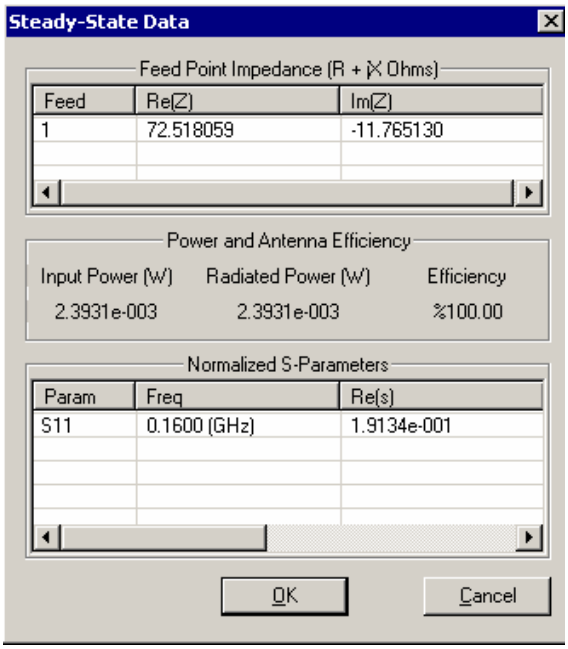

Total E-field **Total H-field**

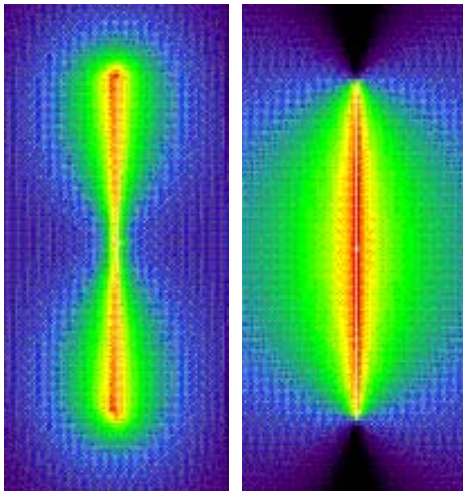

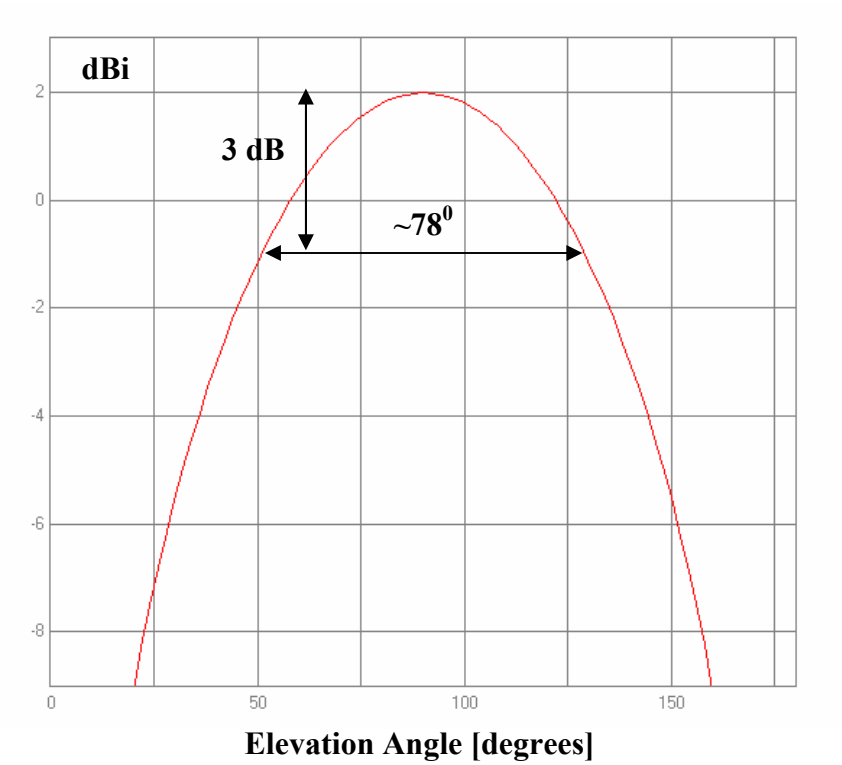

We also compared the XFDTD™ result with the results derived from NEC [4], which is a code based on the method of moments. In this case, we used a dipole with radius 1 mm, length 88.5 cm, and the discretization is 5 mm. The corresponding input impedance at 160 MHz is 69.5-j10.5 ohm. Its frequency dependence is reported in the following figure.

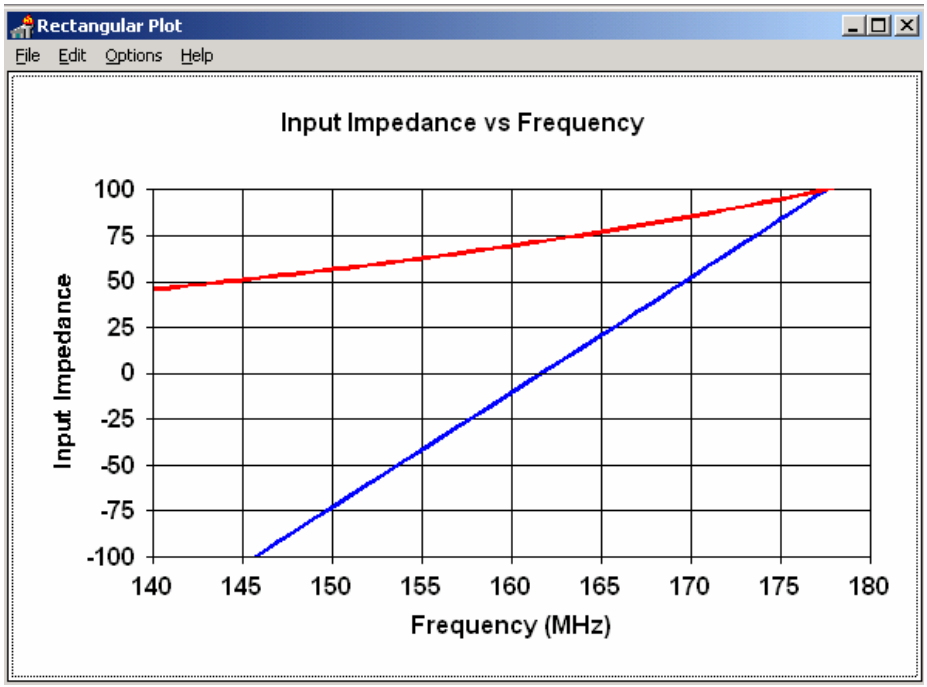

This validation ensures that the input impedance calculation is carried out correctly in XFDTD™, thereby enabling accurate estimates of the radiated power. It further ensures that the wire model employed in XFDTD™, which we used to model the antennas, produces physically meaningful current and fields distributions. Both these aspects ensure that the field quantities are correctly computed both in terms of absolute amplitude and relative distribution.

3) Computational parameters

a) The following table reports the main parameters of the FDTD model employed to perform our computational analysis:

PARAMETER	X	Y	Z
Voxel size	5 mm	5 mm	5 mm
Maximum domain dimensions employed for bystander computations (in voxels)	507	530	432
Maximum domain dimensions employed for passenger computations (in voxels)	400	579	430
Time step	Exactly equal to Courant limit (typically 10 *ps* at this frequency, with the body model)		
Objects separation from FDTD boundary (voxels)	>10	>10	>10
Number of time steps for passenger	At least 7000 in all simulations		

Number of time steps for bystander	At least 6000 in all simulations
Excitation	Sinusoidal (approx. 9-10 periods)

b) In order to fit the model within a grid size that would not use up the available memory, we chopped the hood of the car and the feet of the human model.

4) Phantom model implementation and validation

a) The FDTD mesh of a male human body was created using digitized data in the form of transverse color images. The data is from the *visible human project* sponsored by the National Library of Medicine (NLM) and is available via the Internet (http://www.nlm.nih.gov/research/visible/visible_human.html). The male data set consists of MRI, CT and anatomical images. Axial MRI images of the head and neck and longitudinal sections of the rest of the body are available at 4 mm intervals. The MRI images have 256 pixel by 256 pixel resolution. Each pixel has 12 bits of gray tone resolution. The CT data consists of axial CT scans of the entire body taken at 1 mm intervals at a resolution of 512 pixels by 512 pixels where each pixel is made up of 12 bits of gray tone. The axial anatomical images are 2048 pixels by 1216 pixels where each pixel is defined by 24 bits of color. The anatomical cross sections are also at 1 mm intervals and coincide with the CT axial images. There are 1871 cross sections. The XFDTD™ High Fidelity Body Mesh uses 5x5x5 mm cells and has dimensions 136 x 87 x 397. Dr. Michael Smith and Dr. Chris Collins of the Milton S. Hershey Medical Center, Hershey, Pa, created the High Fidelity Body mesh. Details of body model creation are given in the *methods* section in [5]. The body mesh contains 23 tissues materials. Measured values for the tissue parameters for a broad frequency range are included with the mesh data. The correct values are interpolated from the table of measured data and entered into the appropriate mesh variables. The tissue conductivity and permittivity variation *vs.* frequency is included in the XFDTD™ calculation by a multiple-pole approximation to the Cole-Cole approximated tissue parameters reported by Camelia Gabriel, Ph.D., and Sami Gabriel, M. Sc. (http://www.brooks.af.mil/AFRL/HED/hedr/reports/dielectric/home.html).

In order to fit the car and bystander model within the volume allowed by the available RAM, the feet of the XFDTD™ High Fidelity Body Mesh were cut away, thereby reducing the model length by about 16 cm (32 voxels). Notice that the original model's feet are not flat and parallel to ground as if he were standing, but are inclined downwards. Therefore, we estimated that the actual reduction in body length is 9 cm. The following figure shows the cross section of the model used in the bystander computations, compared with the original XFDTD™ High Fidelity Body Mesh.

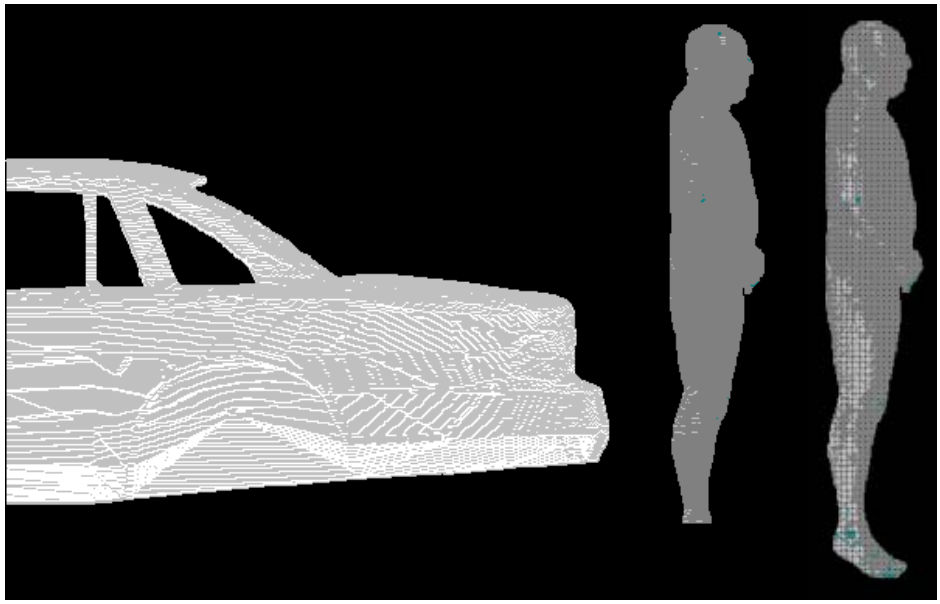

b) The XFDTD™ High Fidelity Body Mesh model correctly represents the anatomical structure and the dielectric properties of body tissues, so it is appropriate for determining the highest exposure expected for normal device operation.

c) One example of the accuracy of XFDTD™ for computing SAR has been provided in [6]. The study reported in [6] is relative to a large-scale benchmark of measurement and computational tools carried out within the IEEE Standards Coordinating Committee 34, Sub-Committee 2.

5) Tissue dielectric parameters

a) The following table reports the dielectric properties used by XFDTD™ for the 23 body tissue materials in the High Fidelity Body Mesh at 155 MHz (mid-band for this VHF mobile radio product).

#	Tissue	ε_r	σ (S/m)	Density (kg/m^3)
1	skin	50.5	0.49	1125
2	tendon, pancreas, prostate, aorta, liver, other	59.3	0.63	1151
3	fat, yellow marrow	5.8	0.04	943
4	cortical bone	15.5	0.08	1850
5	cancellous bone	26.0	0.17	1080
6	blood	64.5	1.65	1057
7	muscle, heart, spleen, colon, tongue	73.6	0.84	1059
8	gray matter, cerebellum	71.5	0.73	1035.5
9	white matter	51.4	0.41	1027.4
10	CSF	73.9	2.29	1000
11	sclera/cornea	61.8	0.94	1151

12	vitreous humor	68.6	1.52	1000
13	bladder	19.1	0.28	1132
14	nerve	44.0	0.41	1112
15	cartilage	53.8	0.53	1171
16	gall bladder bile	86.6	1.49	928
17	thyroid	65.9	0.71	1035.5
18	stomach/esophagus	78.5	1.03	1126
19	lung	52.3	0.59	563
20	kidney	72.9	1.02	1147
21	testis	72.6	0.99	1158
22	lens	57.3	0.61	1163
23	small intestine	89.5	1.85	1153

b) The tissue types and dielectric parameters used in the SAR computation are appropriate for determining the highest exposure expected for normal device operation, because they are derived from measurements performed on real biological tissues (http://www.brooks.af.mil/AFRL/HED/hedr/reports/dielectric/home.html).

c) The tabulated list of the dielectric parameters used in phantom models is provided at point 5(a). As regards the device (car plus antenna), we used perfect electric conductors.

6) Transmitter model implementation and validation

a) The essential features that must be modeled correctly for the particular test device model to be valid are:

- Car body. We developed one very similar to the car used for MPE measurements, so as to be able to correlate measured and simulated field values. The model was imported in XFDTD™ from a CAD model that is commercially available at http://www.3dcadbrowser.com/
- Antenna. We used a straight wire in all cases, even though the gain antenna has a base coil for tuning. All the coil does is compensating for excess capacitance due to the antenna being slightly longer than half a wavelength. We do not need to do that in the model, as we used normalization with respect to the net radiated power, which is determined by the input resistance only. In this way, we neglect mismatch losses and artificially produce an overestimation of the SAR, thereby introducing a conservative bias in the model.
- Antenna location. We used the same location, relative to the edge of the car trunk, the backseat, or the roof, used in the MPE measurements. The following pictures show a lateral and a perspective view of the whole model (XFDTD™ does not show wires in this type of view, that is why the antenna is not visible).

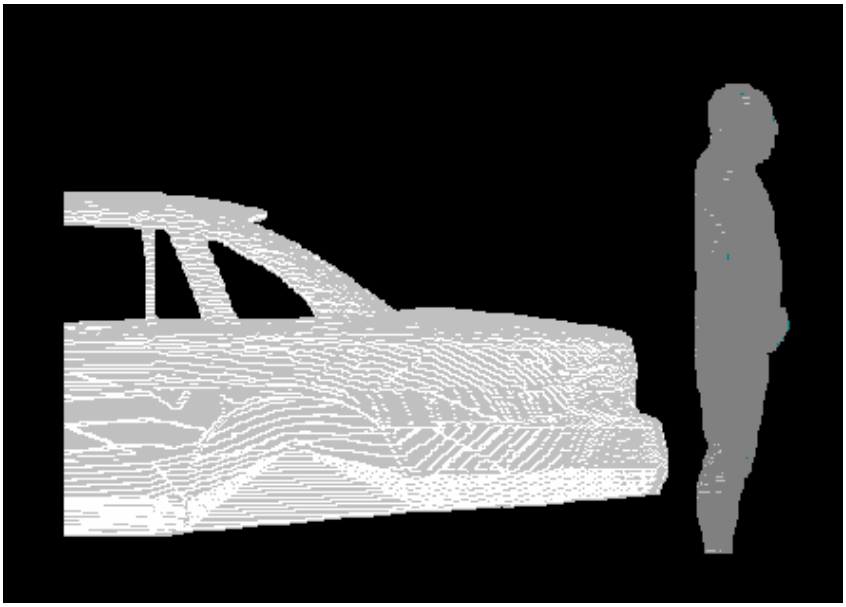

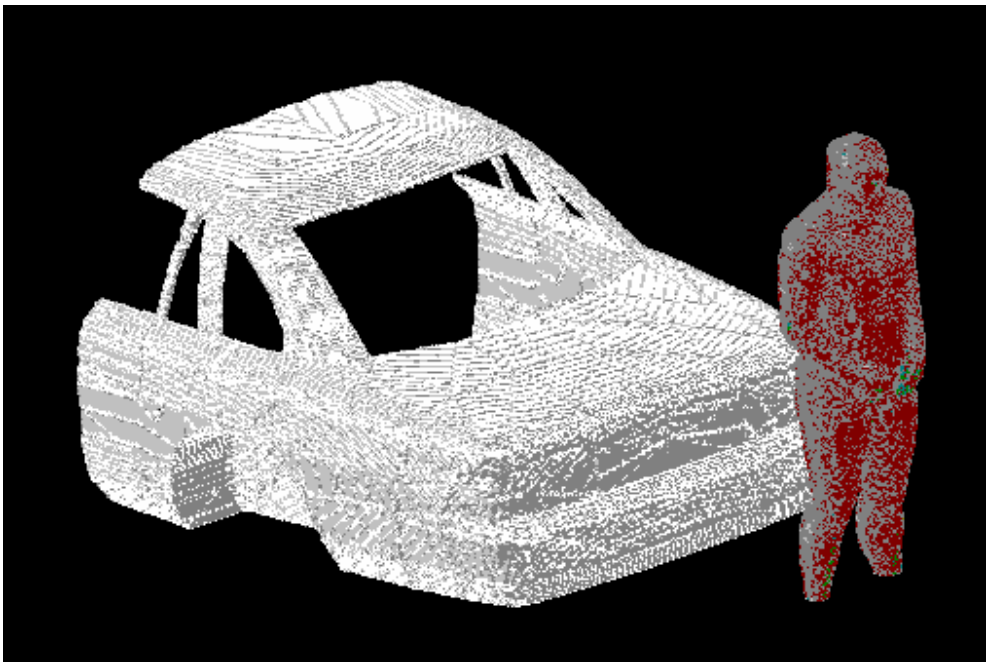

The car model is constituted by perfect electric conductor and does not include wheels in order to reduce its complexity. The passenger model is surrounded by air, as the seat, which is made out of poorly conductive fabrics, is not included in the computational model. The pavement has not been included in the model. The passenger and bystander models were validated for similar antenna and frequency conditions by comparing the MPE measurements at two VHF frequencies (146 MHz and 164 MHz) for antennas used for a VHF mobile radio analyzed previously in 2003 (FCC ID#ABZ99FT3046). The corresponding MPE measurements are reported in the compliance report relative to FCC ID#ABZ99FT3046. The comparison results are presented below, according to following definitions for the equivalent power densities (based on E or H-field):

$$S_E = \frac{|\mathbf{E}|^2}{2\eta}, \quad S_H = \frac{\eta}{2}|\mathbf{H}|^2, \quad \eta = 377\ \Omega$$

<u>Passenger with 43 cm monopole antenna (HAD4009A 164 MHz)</u>

The following figures of the test model show the empty car model, where the yellow dotted line represents the back seat, as it can be observed from the right-hand side figure showing the passenger. The comparison has been performed by taking the computed steady-state field values at the locations corresponding to the head, chest, and legs along the yellow line and comparing them with the corresponding measurements. Such a comparison is carried out at the same rms power level (56.5 W) used in the measurements. Steady-state E-field and H-field distributions at a vertical plane transverse to the car and crossing the passenger's head are displayed as well. Finally, a picture of the antenna is shown.

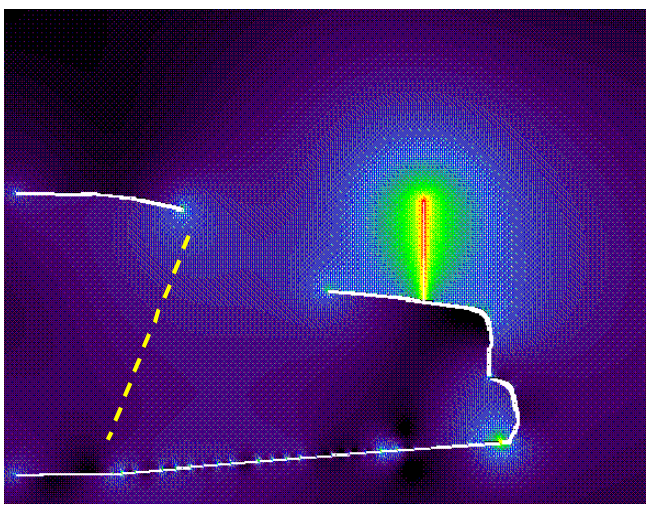

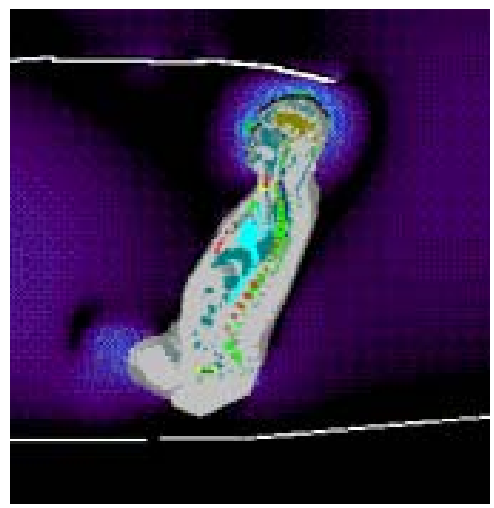

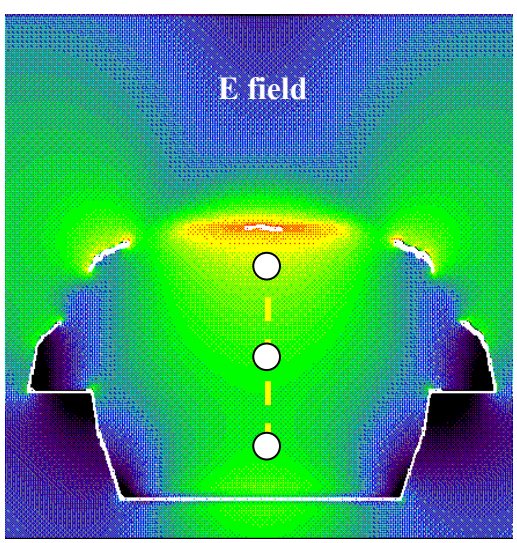

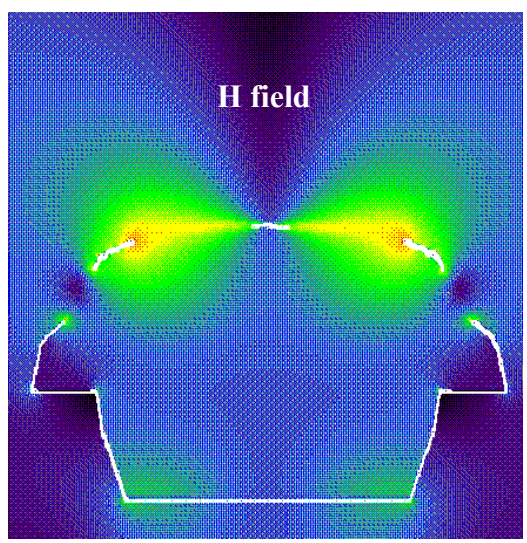

The highest exposure occurs in the middle of the backseat, which is also the case in the measurements. Therefore, the field values were determined on the yellow line centered at the middle of the backseat, approximately at the three locations that are shown by white dots. In actuality, the line is inclined so as to follow the inclination of the passenger's back, as shown previously.

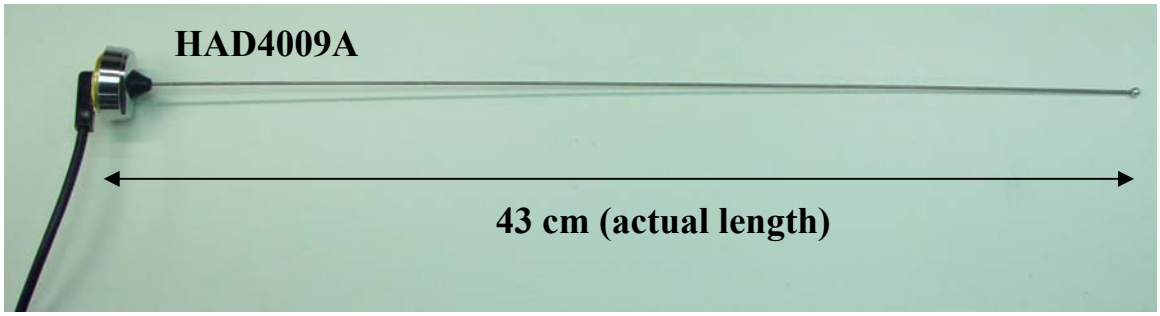

Because the peak exposure occurs in the center of the back seat, that was where we placed the passenger model to perform the SAR evaluations presented in the report. However, it can be observed that the H-field distribution features peaks near the lateral edges of the rear window. That is the reason why we also carried out one SAR computation by placing the passenger laterally in the back seat, in order to determine whether the SAR would be higher in this case.

As done in the measurements, the equivalent power density (S) is computed from the E-field, the H-field being much lower. The following table reports the E-field values computed by XFDTD™ at the three locations, and the corresponding power density.

Location	E-field magnitude (V/m)	S (W/m^2)
Head	1.0	1.33E-03
Chest	0.45	2.69E-04
Lower Trunk area	0.32	1.36E-04
	Average S	**5.77E-04**

The input impedance is 28.2-j27 ohm, therefore the radiated power (considering the mismatch to the 50 ohm unitary voltage source) is 2.06E-3 W. The scaled-up power density for 56.5 W radiated power is 15.8 W/m^2, corresponding to 1.58 mW/cm^2. Measurements gave an average of 1.29 mW/cm^2, which is in good agreement. The following table and the graph show a comparison between the simulated power density and the measured one (see also MPE report in FCC ID#ABZ99FT3046, Table 43), normalized to 56.5 W radiated.

Position	SE (meas) mW/cm^2	SE (FDTD) mW/cm^2
Head	2.98	3.64
Chest	0.74	0.74
Lower Trunk	0.14	0.37

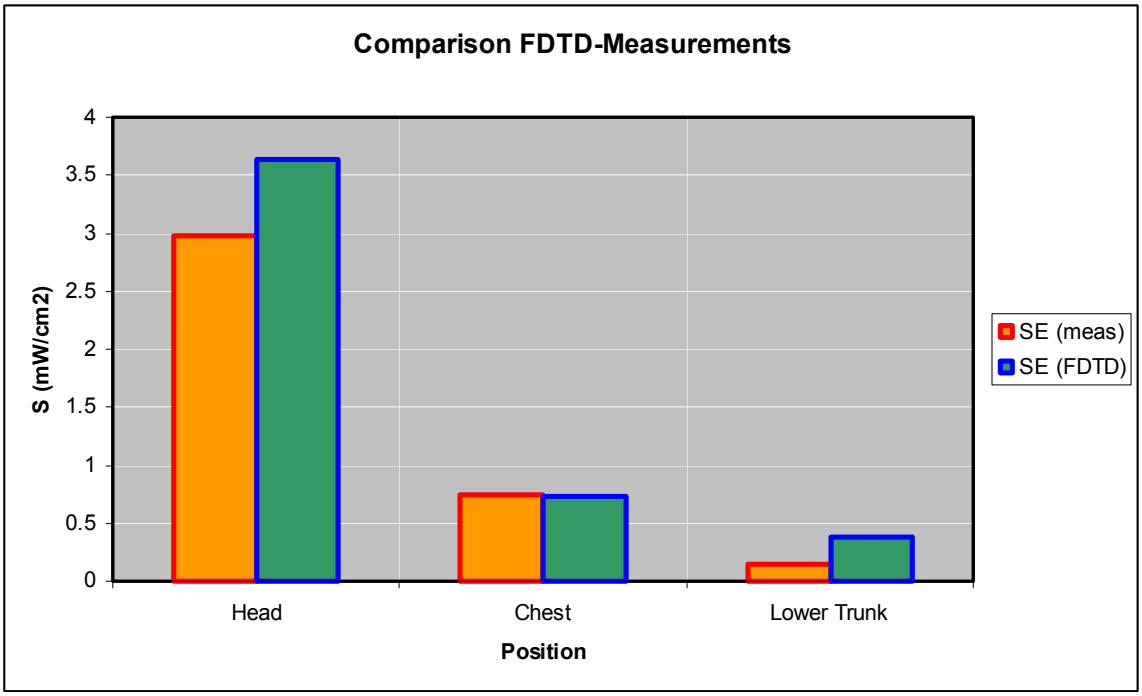

Bystander with 48 cm monopole antenna (HAD4007A 146 MHz)

The following figures show the E-field and H-field distributions across a vertical plane passing for the antenna and cutting the car in half. As done in the measurements, the MPE is computed from both E-field and H-field distributions, along the yellow dotted line at 10 points spaced 20 cm apart from each other up to 2 m in height. These lines and the field evaluation points are approximately indicated in the figures. The E-field and H-field distributions in the vertical plane placed at 60 cm from the antenna, behind the case, are shown as well. The points where the fields are sampled to determine the equivalent power density (S) are approximately indicated by the white dots. A picture of the antenna is not reported because it is identical to the HAD4009A except for the length.

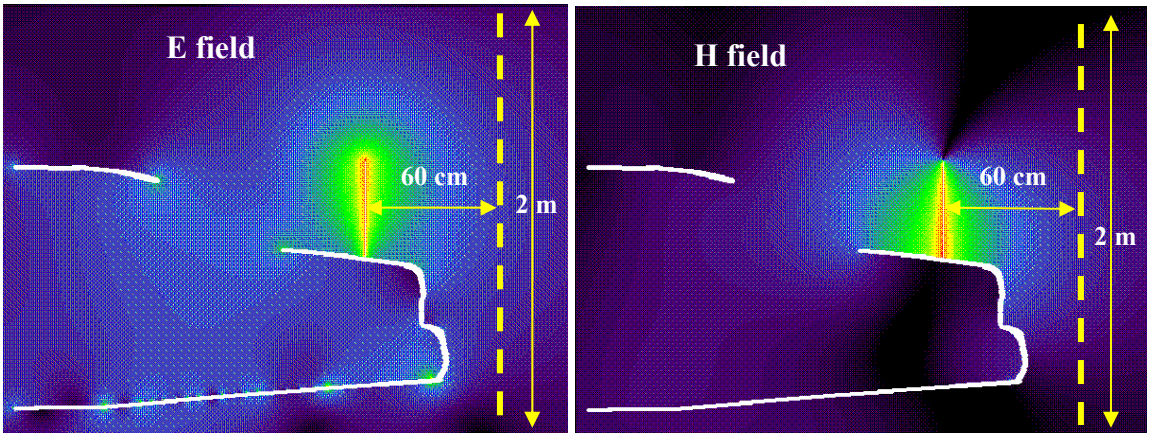

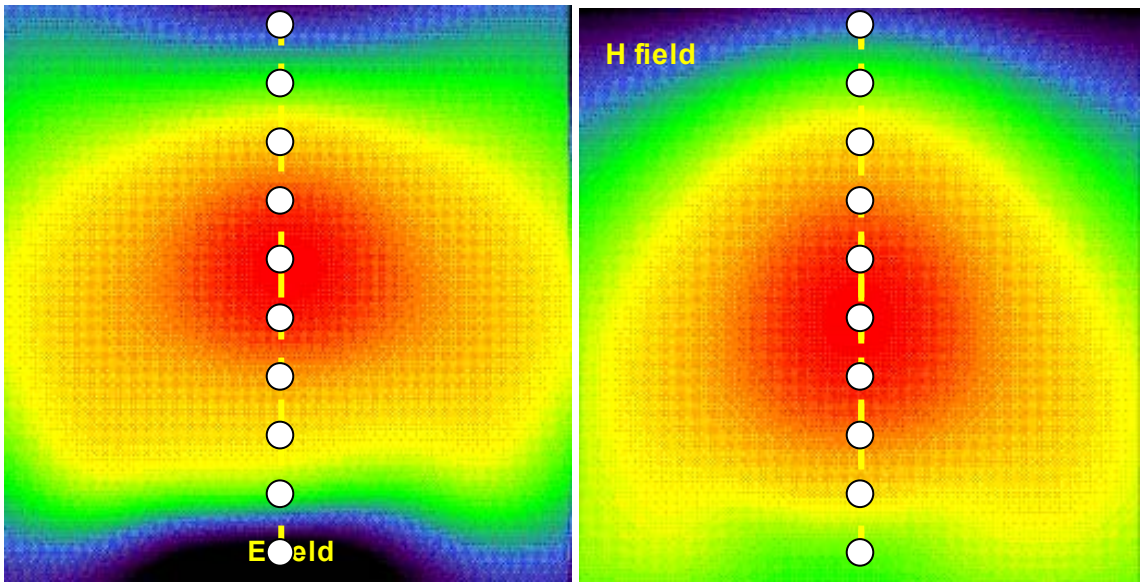

The following table reports the field values computed by XFDTD™ and the corresponding power density values. The average exposure levels are computed as well.

Height (cm)	E (V/m)	S_E (W/m^2)	H (A/m)	S_H (W/m^2)
20	2.12E-01	5.96E-05	5.14E-04	4.98E-05
40	3.81E-01	1.93E-04	8.67E-04	1.42E-04
60	4.43E-01	2.60E-04	1.35E-03	3.45E-04
80	5.36E-01	3.81E-04	1.73E-03	5.67E-04
100	6.17E-01	5.05E-04	1.84E-03	6.37E-04
120	6.28E-01	5.23E-04	1.57E-03	4.63E-04
140	5.59E-01	4.14E-04	1.11E-03	2.34E-04
160	4.41E-01	2.58E-04	6.99E-04	9.20E-05
180	3.24E-01	1.39E-04	3.73E-04	2.63E-05
200	2.31E-01	7.08E-05	1.86E-04	6.54E-06
	Average S_E	**2.80E-04**	**Average S_H**	**2.56E-04**

The input impedance is 27.3-j19.5 ohm, therefore the radiated power (considering the mismatch to the 50 ohm unitary voltage source) is 2.15E-3 W. The scaled-up power density values for 53.2 W radiated power are 6.93 W/m^2 (E), and 6.533 W/m^2 (H), that correspond to 0.69 mW/cm^2 (E), and 0.63 mW/cm^2 (H). Measurements yielded average power density of 0.664 mW/cm^2 (E), and 0.471 mW/cm^2 (H), i.e., which are in good agreement with the simulations. The following table and graph show a comparison between the simulated power density and the measured one, based on E (see MPE report in FCC ID#ABZ99FT3046, Table 1) or H fields (see MPE report in FCC ID#ABZ99FT3046, Table 13), normalized to 53.2 W radiated.

Height (cm)	SE (meas) mW/cm^2	SE (FDTD) mW/cm^2	SH (meas) mW/cm^2	SH (FDTD) mW/cm^2	Avg SE meas mW/cm^2	Avg SE FDTD mW/cm^2	Avg SH meas mW/cm^2	Avg SH FDTD mW/cm^2
20	0.19	0.15	0.2	0.12	0.664	0.694	0.471	0.634
40	0.37	0.48	0.23	0.35				
60	0.55	0.64	0.3	0.85				
80	0.68	0.94	0.56	1.40				
100	1.02	1.25	1.07	1.58				
120	1.15	1.29	1.1	1.15				
140	1.04	1.03	0.56	0.58				
160	0.79	0.64	0.24	0.23				
180	0.5	0.34	0.23	0.06				
200	0.35	0.18	0.22	0.02				

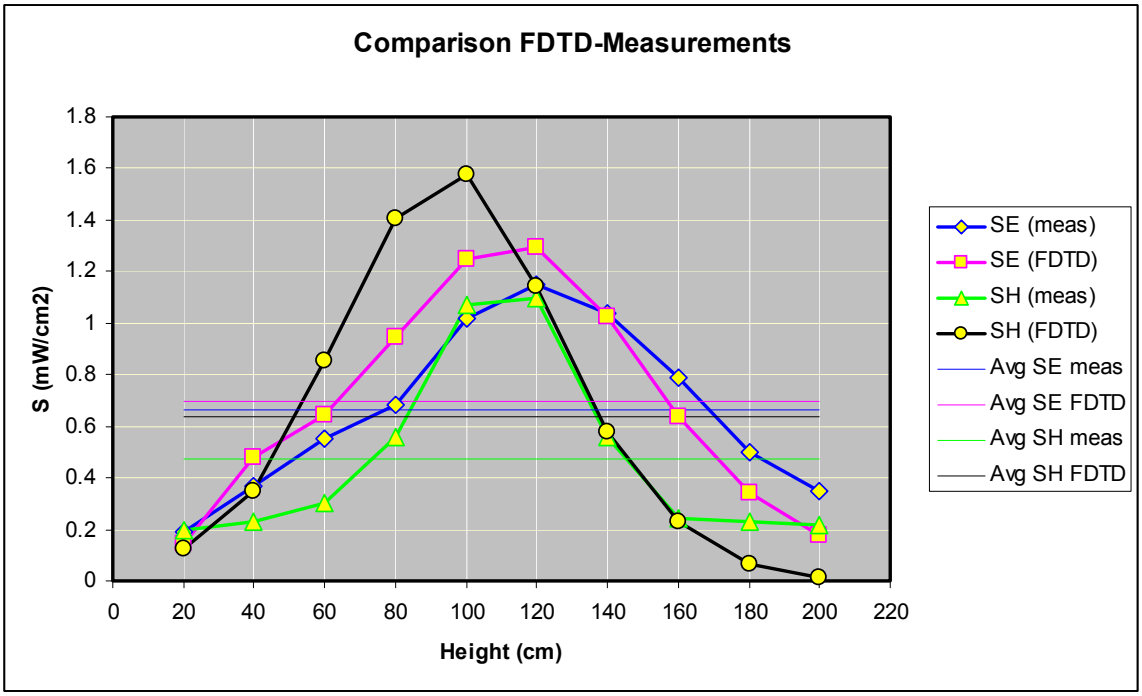

7) Test device positioning

a) A description of the device test positions used in the SAR computations is provided in the SAR report.

b) Illustrations showing the separation distances between the test device and the phantom for the tested configurations are provided in the SAR report.

8) Steady state termination procedures

a) The criteria used to determine that sinusoidal steady-state conditions have been reached throughout the computational domain for terminating the computations are based on the monitoring of field points to make sure they converge. For at least one passenger and one bystander exposure condition, we placed one "field sensor" near the antenna, others between the body and the domain boundary at different locations, and one inside the head of the model. In all simulations, isotropic E-field sensors were placed at opposite corners of the computational domain. We used isotropic E and H field "sensors", meaning that all three components of the fields are monitored at these points. The following figures show an example of the time waveforms at the field point sensors in the head and in two opposite points in the computational domain. In the latter case, we selected points near the lowest and highest grid index points. They are shown together in the figure. The highest field levels are observed for the higher index point, as it is closer to the antenna. In all cases, the field reaches the steady-state after a few cycles.

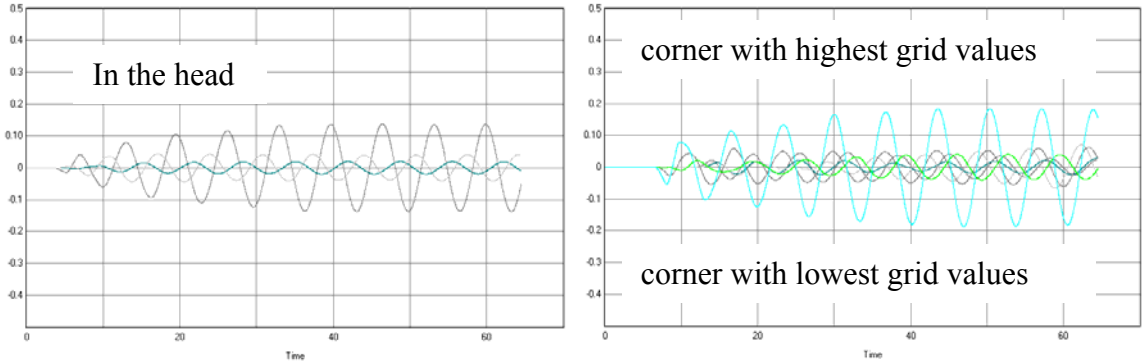

b) 6000 to 7500 time steps were used, with a time step approximately equal to 10 *ps* (meeting the Courant criterion), which corresponds to 9-11 wave periods at 149 MHz. Bystander case involves more steps because the simulation domain is larger.

c) The XFDTD™ algorithm determines the field phasors by using the so-called "two-equations two-unknowns" method. Details of the algorithm are explained in [7].

9) Computing peak SAR from field components

a) The twelve E-field phasors at the edges of each Yee voxel are combined to yield the SAR associated to that voxel. In particular, the average is performed on the SAR values computed at the 12 edges of each voxel. Notice that in XFDTD™ the dielectric tissue

properties are assigned to the voxel edges, thereby allowing said averaging procedure.

b) The IEEE Standards Coordinating Committee 34, Sub-Committee 2 draft standard P1529 (June 2000) discusses several algorithms for volumetric SAR averaging. It states that "It is observed that while the 12 components algorithm is the most appropriate from the mathematical point of view, the differences in 1g SAR calculated with either the 12 or 6 component methods are negligible for practical mesh resolutions (below 5mm). On the other hand, it is shown that the 3 components approach may lead to significant errors." XFDTD™ employs the 12-component method, which is the one recommended in the draft standard, thus providing the best achievable accuracy.

10) One-gram averaged SAR procedures

a) XFDTD™ computes the Specific Absorption Rate (SAR) in each complete cell containing lossy dielectric material and with a non-zero material density. To be considered a complete cell, the twelve cell edges must belong to lossy dielectric materials. The averaging calculation uses an interpolation scheme for finding the averages. Cubical spaces centered on a cell are formed and the mass and average SAR of the sample cubes are found. The size of the sample cubes increases until the total mass of the enclosed exceeds either 1 or 10 grams. The mass and average SAR value of each cube is saved and used to interpolate the average SAR values at either 1 or 10 grams. The interpolation is performed using two methods (polynomial fit and rational function fit) and the one with the lowest error is chosen. The sample cube must meet some conditions to be considered valid. The cube may contain some non-tissue cells, but some checks are performed on the distribution of the non-tissue cells. A valid cube will not contain an entire side or corner of non-tissue cells.

b) The sample cube increases in odd-numbered steps (1x1x1, 3x3x3, 5x5x5, etc) to remain centered on the desired cell. Since the visible human model employed herein has 5 mm resolution, the one-gram SAR is computed by averaging first over 1x1x1 voxels, corresponding to 0.125 cm^3 (not enough yet), and then over a 3x3x3 voxel cube, corresponding to about 3.4 cm^3, which is enough to include 1-g, and finally over a 5x5x5 voxel cube, corresponding to about 15.6 cm^3, which includes 10-g. The 1-g average SAR is computed by interpolating these three data points. This procedure is repeated in the surroundings of each voxel that is constituted by lossy materials, so as to determine the 1-g and/or 10-g SAR distributions.

c) As mentioned at points 10(a) and 10(b), the 1- gram average SAR is determined by interpolating the average SAR for the 1x1x1 , 3x3x3, and the 5x5x5 data points, corresponding to 0.125 cm^3, 3.4 cm^3, and 15.6 cm^3, respectively. Because the interpolation is carried out across three data points, the error introduced should be negligible because the interpolating curve crosses exactly the data points.

11) Total computational uncertainty – We derived an estimate for the uncertainty of FDTD methods in evaluating SAR by referring to [6]. In Fig. 7 in [6] it is shown that the deviation between SAR estimates using the XFDTD™ code and those measured with a

compliance system are typically within 10% when the probe is away from the phantom surface so that boundary effects are negligible. In that example, the simulated SAR always exceeds the measured SAR.

As discussed in 6(a), a conservative bias has been introduced in the model so as to reduce concerns regarding the computational uncertainty related to the car modeling, antenna modeling, and phantom modeling. The results of the comparison between measurements and simulations presented in 6(a) suggest that the present model produces an overestimate of the exposure between 4% and 36%. Such a conservative bias should eliminate the need for including uncertainty considerations in the SAR assessment.

12) Test results for determining SAR compliance

a) Illustrations showing the SAR distribution of dominant peak locations produced by the test transmitter, with respect to the phantom and test device, are provided in the SAR report.

b) The input impedance and the total power radiated under the impedance match conditions that occur at the test frequency are provided by XFDTD™. XFDTD™ computes the input impedance by following the method outlined in [8], which consists in performing the integration of the steady-state magnetic field around the feed point edge to compute the steady-state feed point current (I), which is then used to divide the feed-gap steady-state voltage (V). The net *rms* radiated power is computed as

$$P_{XFDTD} = \frac{1}{2}\mathrm{Re}\left\{VI^*\right\}$$

Both the input impedance and the net rms radiated power are provided by XFDTD™ at the end of each individual simulation.

We normalize the SAR to such a power, thereby obtaining SAR per radiated Watt (*normalized SAR*) values for the whole body and the 1-g SAR. Finally, we multiply such normalized SAR values times the max power rating of the device under test. In this way, we obtain the exposure metrics for 100% talk-time, i.e., without applying source-based time averaging.

c) For mobile radios, 50% source-based time averaging is applied by multiplying the SAR values determined at point 12(b) times a 0.5 factor.

REFERENCES

[1] K. S. Yee, "Numerical Solution of Initial Boundary Value Problems Involving Maxwell's Equations in Isotropic Media," *IEEE Transactions on Antennas and Propagation*, vol. 14, no. 3, 302-307, March 1966.

[2] Z. P. Liao, H. L. Wong, G. P. Yang, and Y. F. Yuan, "A transmitting boundary for transient wave analysis," Scientia Sinica, vol. 28, no. 10, pp 1063-1076, Oct. 1984.

[3] Validation exercise: Mie sphere. Remcom Inc. (enclosed PDF)

Remcom.pdf

[4] NEC-Win PRO ™ v 1.1, Nittany Scientific, Inc., Riverton, UT.

[5] C. M. Collins and M. B. Smith, "Calculations of B1 distribution, SNR, and SAR for a surface coil against an anatomically-accurate human body model," *Magn. Reson. Med.*, 45:692-699, 2001. (enclosed TIF)

Collins & Smith.pdf

[6] Martin Siegbahn and Christer Törnevik, "Measurements and FDTD Computations of the IEEE SCC 34 Spherical Bowl and Dipole Antenna," Report to the IEEE Standards Coordinating Committee 34, Sub-Committee 2, 1998. (enclosed PDF)

Ericsson.pdf

[7] C. M. Furse and O. P. Gandhi, "Calculation of electric fields and currents induced in a millimeter-resolution human model at 60 Hz using the FDTD method with a novel time-to-frequency-domain conversion," Antennas and Propagation Society International Symposium, 1996. (enclosed PDF)

Furse & Gandhi.pdf

[8] *The Finite Difference Time Domain Method for Electromagnetics*, Chapter 14.2, by K. S. Kunz and R. J. Luebbers, CRC Press, Boca Raton, Florida, 1993.

Validation Exercise: Layered Lossy Dielectric Sphere

- Inner radius: 6.25 cm, outer radius: 8.33 cm
- Frequency: 1.9 GHz, ? = 15.8 cm
- 1.28 mm FDTD cells, about 6×10^6 cells total, 4000 time steps
- Outer spherical shell: relative permittivity of 10, ? = 0.5 S/m
- Inner sphere: relative permittivity of 20, ? = 0.5 S/m
- Plane wave excitation
- FDTD results are compared to exact modal solution

Validation Exercise: Layered Lossy Dielectric Sphere

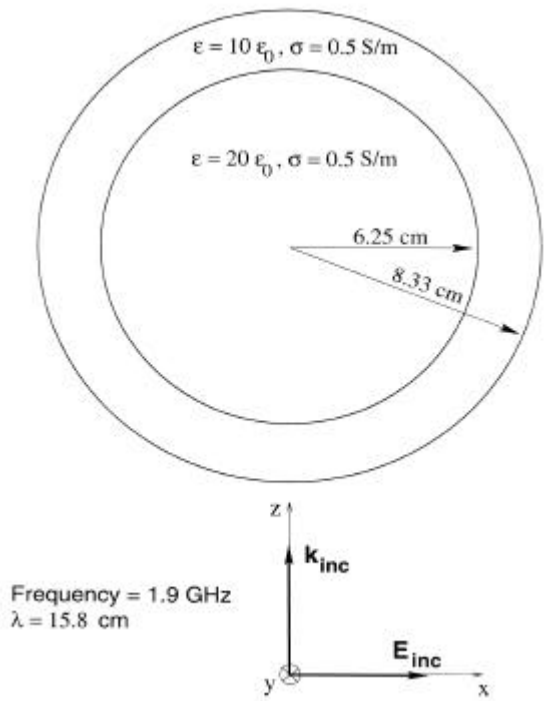

Validation Exercise: Lossy Dielectric Sphere

Modal Solution for E-Field Magnitude

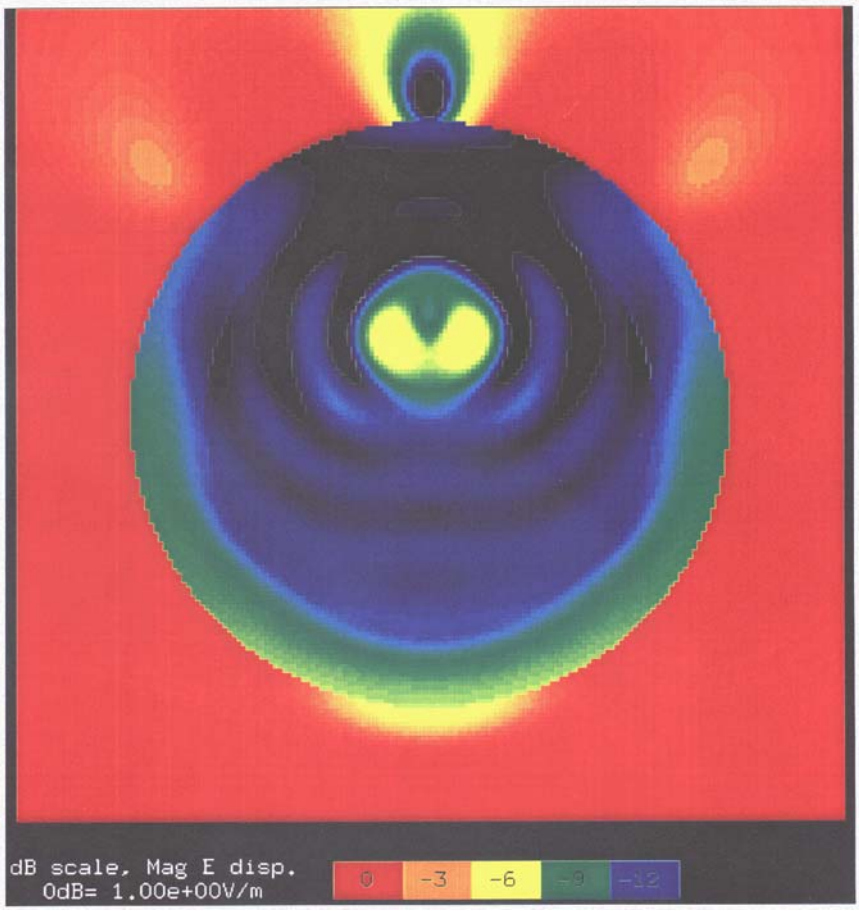

Validation Exercise: Lossy Dielectric Sphere

FDTD Solution for E-Field Magnitude

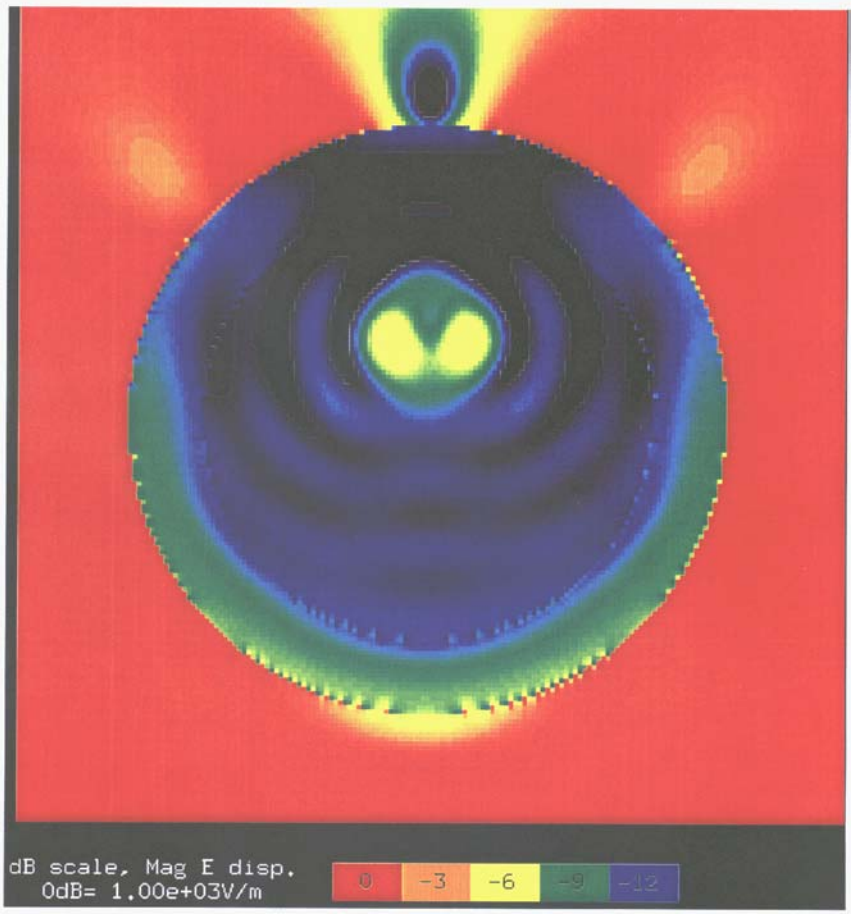

Magnetic Resonance in Medicine 45:692–699 (2001)

Calculations of B_1 Distribution, SNR, and SAR for a Surface Coil Adjacent to an Anatomically-Accurate Human Body Model

Christopher M. Collins[1,3] and Michael B. Smith[1,2*]

Calculations of the radiofrequency magnetic (B_1) field, SAR, and SNR as functions of frequency between 64 and 345 MHz for a surface coil against an anatomically-accurate human chest are presented. Calculated B_1 field distributions are in good agreement with previously-published experimental results up to 175 MHz, especially considering the dependence of field behavior on subject anatomy. Calculated SNR in the heart agrees well with theory for low frequencies (nearly linear increase with B_0 field strength). Above 175 MHz, the trend in SNR with frequency begins to depend largely on location in the heart. At all frequencies, present limits on local (1 g) SAR levels are exceeded before limits on whole-body average limits. At frequencies above 175 MHz, limits on SAR begin to be an issue in some common imaging sequences. These results are relevant for coils and subjects similar to those modeled here. Magn Reson Med 45:692–699, 2001. © 2001 Wiley-Liss, Inc.

Key words: calculations; SNR; power; MRI; high field

The desire for a greater signal-to-noise ratio (SNR) in magnetic resonance spectroscopy (MRS) and imaging of humans continues to fuel interest in MR research at increasing static magnetic (B_0) field strengths, and consequently with increasing radiofrequency (RF) magnetic (B_1) field frequencies. As B_1 frequency increases, the spatial distribution of the B_1 field in a given object becomes more complex. This makes predictions of both SNR and the specific absorption rate (SAR) more difficult. Although at frequencies up to 64 MHz a nearly linear increase in SNR with B_0 field strength is expected theoretically (1–3) and seen experimentally (2) in human geometries, prediction of SNR at frequencies higher than this requires consideration of all of Maxwell's equations in 3D structures similar to those of interest in experiment (4–10).

Calculations of the B_1 field patterns, SAR, and SNR as functions of frequency for a surface coil used for both transmit and receive against the human chest are presented here. Calculations were performed in such a way as to make comparison to previous experiments (11) possible, and results of SAR calculations are presented in a manner that should make prediction of SAR in particular experiments with a similar coil and subject possible.

[1]Department of Radiology, Pennsylvania State University College of Medicine, Hershey, Pennsylvania.

[2]Department of Physiology, Pennsylvania State University College of Medicine, Hershey, Pennsylvania.

[3]Department of Bioengineering, University of Pennsylvania, Philadelphia, Pennsylvania.

*Correspondence to: Michael B. Smith, Center for NMR Research, NMR/MRI Building, Department of Radiology H066, Pennsylvania State University College of Medicine, 500 University Drive, Hershey, PA 17033.
E-mail: mbsmith@psu.edu

Received 17 July 2000; revised 1 November 2000; accepted 8 November 2000.

© 2001 Wiley-Liss, Inc.

METHODS

A model of the human body for use with the finite difference time domain (FDTD) method of numerical calculation for electromagnetics (12,13) was created by first segmenting the digital photographic data of the National Library of Medicine's Visible Male Project, and then creating a 3D grid of Yee cells (13) from the segmented data. The images of the Visible Male Project, with a resolution of 1/3 mm in the left-right (x) and anterior-posterior (y) directions, were segmented at 5-mm intervals in the inferior-superior (z) direction by a fairly manual process, reference to anatomical atlases, and assistance from two practicing radiologists and one medical student. A program was written to create a 3D grid of Yee cell cubes from the segmented images with a spatial resolution of 5 mm in each dimension ($\Delta_x = \Delta_y = \Delta_z = 5$ mm). In a previous study of the relationship between spatial resolution and SAR levels, as calculated in the human head with the FDTD method (14), it was found that maximum local (1 cm^3) SAR values calculated with 8 cells per cm^3 ($\Delta_x = \Delta_y = \Delta_z = 5$ mm) were different from those calculated with 100 cells per cm^3 by less than 20%, and that average SAR values calculated with 8 cells per cm^3 were different from those calculated with 100 cells per cm^3 by less than 7%. Since the layer of skin is very thin in some places, and some information regarding it may be lost in the creation of a model with 5-mm dimensions, a second program was written to ensure that a continuous layer of skin existed by assigning the properties of skin to the surfaces of all Yee cell cubes that are adjacent to air. This step was seen as important because the conductivity of skin is greater than that of the fatty tissue beneath it in most places by a factor of about 10, and skin is typically the closest tissue to the RF coil elements. Thus SAR levels in the skin are generally expected to be relatively high in comparison to other tissues (15). Several slices through the completed model are shown in Fig. 1. In this figure each Yee cell cube (consisting of 12 Yee cell elements, one along each edge of the Yee cell cube) is depicted as a single box, and it appears that the skin is discontinuous in some areas, such as on the anterior surface in the second axial image from the right. Another view of this region showing all Yee cell elements (Fig. 2) reveals that the Yee cell elements representing skin on the outer surface here do indeed form a continuous layer. Values for material density were taken from the literature (16–19), and values for electrical properties were derived at each frequency by linear interpolation from measurements by Gabriel (20) in each tissue.

A circular surface coil with a diameter of 22.9 cm was modeled near the chest of the whole-body model. The coil was placed at a distance of 1 cm from the tissue. This 1-cm

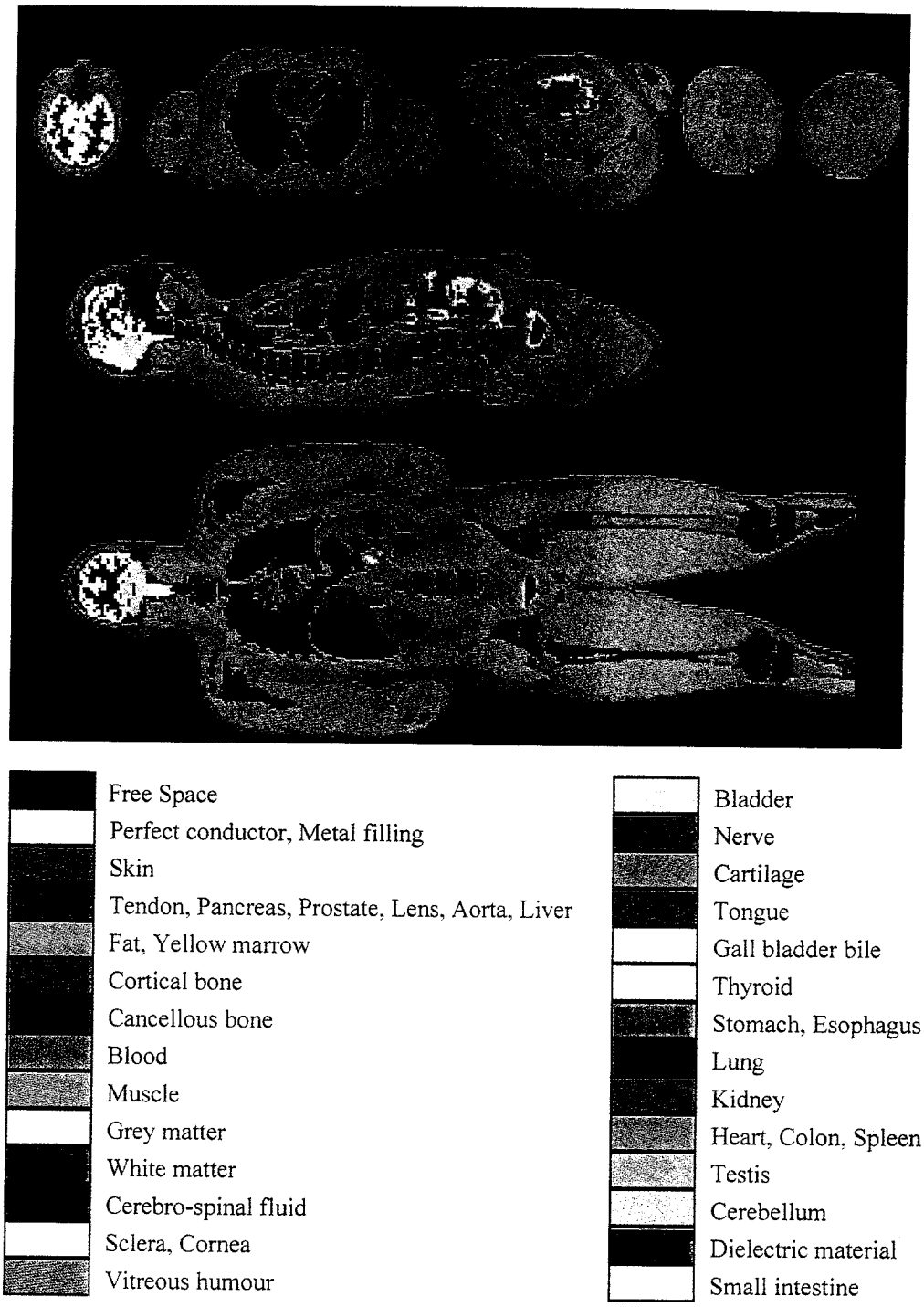

FIG. 1. Slices through a whole-body 3D model with 5-mm resolution in each dimension. Top: Axial slices through the head, thorax, abdomen, and thighs. Middle: Sagittal slice through the middle of body. Bottom: Coronal slice chosen to show the extent of the legs.

distance occurs where the pectoral muscles are more protrusive (left and right of center). Along the sagittal centerline (near the sternum), the distance between the coil and tissue is greater, with the greatest distance being almost 4 cm between the superior arc of the coil and the throat of the human body model. The coil model was driven with four voltage sources spaced evenly about the coil. The four voltage sources had identical magnitude and phase at each frequency. This is consistent with theoretical requirements for resonance of a symmetric four-capacitor coil, provided that the coil is loaded symmetrically and lengths of conductive segments are not long compared to one wavelength at the frequency of interest. This method can therefore be seen as an idealized approximation for this case with asymmetric loading, especially at frequencies of 260 and 345 MHz, where the length of the conductive segments is 0.156 and 0.207 times that of one wavelength, respectively. A surface coil of this size driven at only one

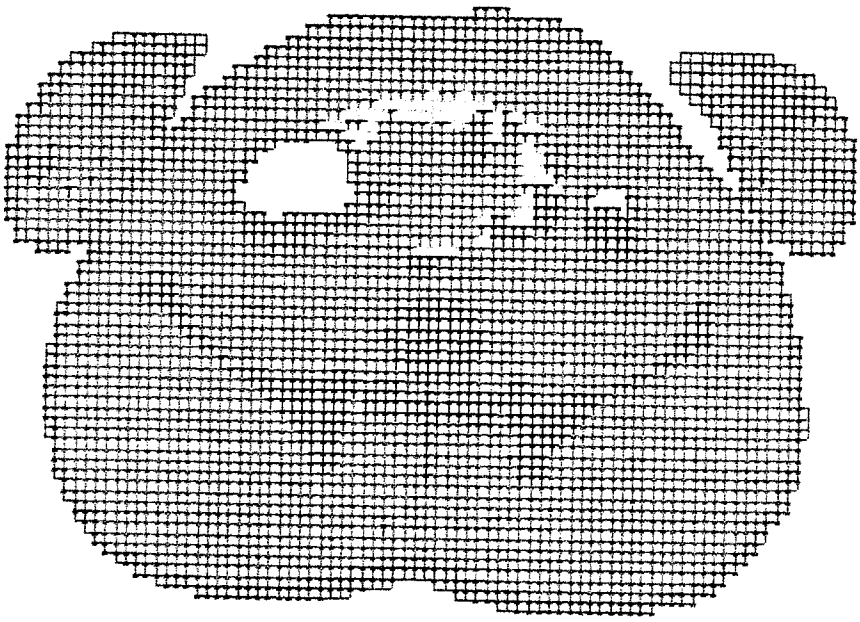

FIG. 2. In a view of an axial slice through the abdomen showing all Yee cell elements (*x*-oriented: horizontal lines, *y*-oriented: vertical lines, *z*-oriented: squares) it is apparent that not all Yee cell elements, such as the skin on the anterior surface of the abdomen, are shown when one Yee cell cube is displayed per pixel, as in Fig. 1.

location at 345 MHz would likely have a less symmetric field distribution than that shown here. Coils can be constructed and driven a number of different ways, however, and it is possible that a coil driven at more than one location could have a very similar field distribution to that shown here. For the purposes of this study, in which we attempted to examine the B_1 field distribution in the presence of a human sample and the effects of this distribution on MRI as functions of frequency, we preferred to keep the coil electrical behavior fairly constant. Electrical behavior of specific coils at these high frequencies, depending on location and number of drive points, type of capacitors (distributed or lumped-element), distance from the chest, and other design considerations should be the subject of future calculations.

All FDTD calculations were set up and performed with the aid of commercially-available software (XFDTD; Remcom, Inc., State College, PA). Calculations of steady-state B_1 fields and SAR were performed at 64, 125, 175, 260, and 345 MHz (corresponding approximately to B_0 field strengths of 1.5, 3.0, 4.0, 6.0, and 8.0 Tesla) with voltage source magnitudes equal to 1 volt. The complex (using phasor notation to include both magnitude and phase) RF electrical field (**E**) vector information and complex RF magnetic field (B_1) vector information at all vertices on the grid of Yee cells were derived from the FDTD calculation results. The amplitudes of the circularly-polarized components of the B_1 field on an axial plane through the chest were then calculated as (21):

$$B_1^+ = |(\hat{B}_x + i\hat{B}_y) \div 2| \qquad [1a]$$

and

$$B_1^- = |(\hat{B}_x - i\hat{B}_y)^* \div 2| \qquad [1b]$$

where $\hat{B}_x$ and $\hat{B}_y$ are complex values as denoted with a circumflex, i is the imagnary unit, the asterisk indicates the complex conjugate, and imaginary components are 90° out of phase with real components at the frequency of interest. Whether B_1^+ or B_1^- is the component that rotates in the direction of nuclear precession and thus induces the flip angle depends on whether the B_0 field is oriented with or against the *z*-axis. In this work it is assumed that B_1^+ is the flip-inducing component.

The dimensionless normalization factor, V, which is necessary to produce a normalized field magnitude, $V B_1^+$, equal to 1.957μT at a point approximately at the center of the heart, was determined at each frequency. This is the field strength necessary to produce a flip angle (α) of 90° in ^{1}H with a 3-msec rectangular RF pulse. Since B_1^+ is associated with driving voltages of 1 volt in the coil, the dimensionless normalization factor V is also equal to the driving voltage (in volts) necessary to produce the field pattern $V B_1^+$.

The available signal from a group of nuclei from a very small volume (cubic voxel, 5-mm dimensions) was assumed to be proportional to the square of the frequency of precession f (1,2), the sine of the flip angle in that volume, and the sensitivity of the coil to the local precessing nuclear magnetism, which is proportional to B_1^- (21). Noise from the sample (the dominant source of noise at these frequencies) is proportional to the square root of the power absorbed by the sample, P_{abs} (2). Thus, neglecting signal from protons in lipid and relaxation effects (T_1 and T_2) for simplicity, SNR at a point near the center of the heart was calculated at each frequency as (21):

$$\mathrm{SNR} \propto f^2 \frac{|\sin(VB_{1c}^-\gamma\tau)B_{1c}^-|}{\sqrt{P_{abs}}} \qquad [2]$$

where B_{1c}^+ is B_1^+ of the center voxel, τ is the duration of the rectangular pulse (assumed to be 3 msec in these calculations), and γ is the gyromagnetic ratio of ^{1}H. P_{abs}, the absorbed power over the entire body, is calculated for use in Eq. [2] as (13):

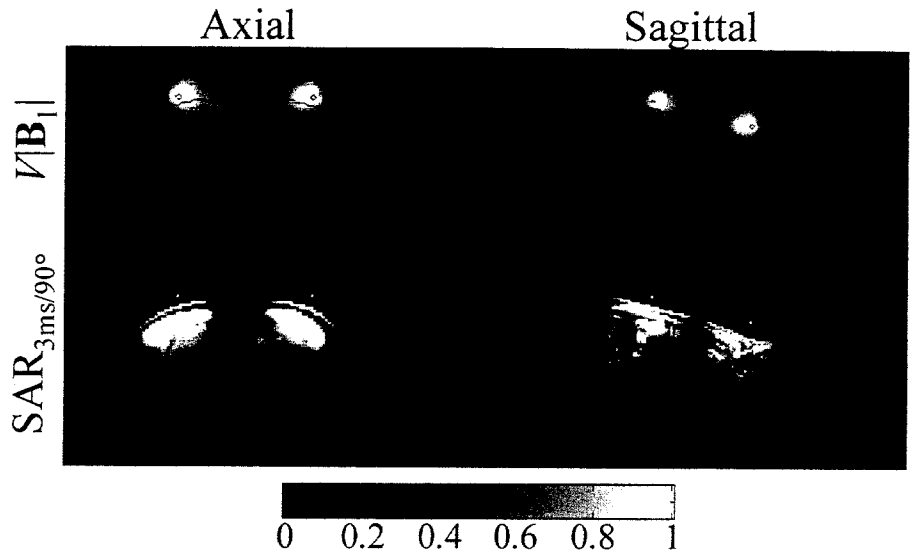

FIG. 3. Distributions of $V|\mathbf{B}_1|$ (top), and $SAR_{3msec/90°}$ (bottom) for body model near surface coil at 64 MHz. Gray scale expressed in terms of fraction of maximum scale value. Maximum scale value is 20μT for $|\mathbf{B}_1|$, and 4.05 W/kg (30 times whole-body average value) for $SAR_{3msec/90°}$. Values above scale maximum are expressed as the same (white) intensity as the scale maximum.

$$P_{abs} = \frac{1}{2}\sum_N (\sigma_{xn}E_{xn}^2 + \sigma_{yn}E_{yn}^2 + \sigma_{zn}E_{zn}^2)\Delta_x\Delta_y\Delta_z \qquad [3]$$

where E_x, E_y, and E_z are the absolute magnitudes of the three orthogonal components of the electrical field E (calculated with the FDTD method), and σ is material conductivity. A dimensional analysis with σ having units of siemens/m, E having units of volts/m, and Δ_x, Δ_y, and Δ_z having units of meters shows the result to have units of watts. The subscript n indicates the nth voxel in the summation, and the subscripts x, y, and z indicate the orientation of the corresponding E field or σ components. The summation is performed over all N voxels in the human body model. Like B_1^+, the values of E and P_{abs} correspond to the fields where $V = 1$.

The SAR during the excitation with $V = 1$ in each voxel in the body model was calculated as (13):

$$SAR_{V=1} = \frac{\sigma_x}{2\rho_x}E_x^2 + \frac{\sigma_y}{2\rho_y}E_y^2 + \frac{\sigma_z}{2\rho_z}E_z^2 \qquad [4]$$

where ρ is the material density (having units of kg/m^3). The SAR during a 3-msec rectangular pulse resulting in a 90° flip at the center of the heart ($SAR_{3msec/90°}$) is equal to $V^2SAR_{V=1}$. For comparison with present limits on SAR (having units of watts/kg), the maximum SAR averaged over any one cm^3 and the average SAR over the entire body model are presented here.

RESULTS AND DISCUSSION

The distribution of $V|\mathbf{B}_1|$ and SAR on two orthogonal planes through the center of the coil at 64 MHz are given in Fig. 3. At 64 MHz the field and $SAR_{3msec/90°}$ distributions are similar to what is expected at lower frequencies (22). Contour plots of the flip angle (α) distribution at each frequency are given in Fig. 4. Numerical values for the normalization factor V, resulting $SAR_{3msec/90°}$ levels (maximum 1 cm^3 and whole-body average), P_{abs}, and SNR are given in Table 1. Line plots of average $SAR_{3msec/90°}$ and SNR as functions of frequency are given in Figs. 5 and 6.

Comparisons of calculated results in this work to previously-published results of Wen et al. (11) suggest that the trends in the B_1 field pattern and SNR with frequency calculated in a human sample are consistent with experiment—at least at frequencies up to 175 MHz. Determination of the accuracy of specific calculated quantities, especially SAR, will likely require further careful experiments and calculations.

Wen et al. (11) published B_1^+ maps made in two different human subjects with a 22.9-cm-diameter surface coil over the chest at 64 MHz (1.5T), 125 MHz (3T), and 175 MHz (4T). Despite differences in body shape and composition between their subjects and our model, calculated contours at α = 45°, 90°, and 180° (Fig. 4) are similar in shape and position to experimentally mapped contours in subject 1 of the study by Wen et al. (Fig. 4 of Ref. 11). In comparing these studies it is important to note that the left-right convention in this work is like that used by radiologists: the "right" side of the model is on the viewer's left. This is the opposite of the convention used by Wen et al. Also, the plane used in calculations (including the atria and ventricular outflow tracts of the heart) may be a centimeter or two (at most) superior to that used in subject 1 of the study by Wen et al. (which apparently includes primarily the ventricles of the heart). Given the substantial differences between the experimentally-measured B_1^+ maps in the two subjects of the study by Wen et al., the presence of the 450° contour in calculations at 64 and 125 MHz (which is absent in subject 1 of the study by Wen et al.) may be attributable to the (apparently) larger pectoral muscles in the model. This will both cause the coil to be farther from the center of the heart than in the experiments by Wen et al., and will require the calculated B_1^+ field to penetrate through more muscle tissue, which is lossier than lung, bone, and fat. Thus higher B_1^+ values near the surface of our model may be necessary in order to achieve a 90° flip at the center of the heart.

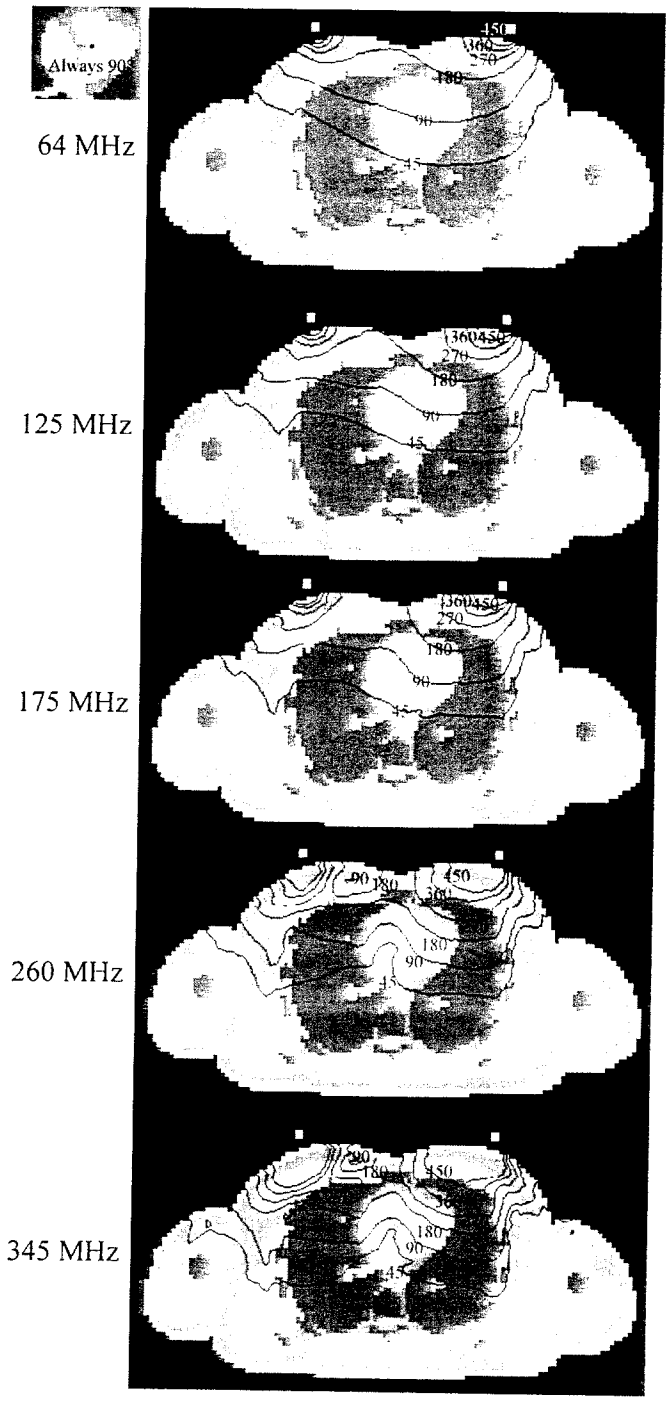

FIG. 4. Distribution of the flip angle α in chest as induced by a surface coil at several frequencies. Location of reference point (where α = 90° at all frequencies) shown in upper-left view of mediastinum. Contours at 45°, 90°, 180°, 270°, 360°, and 450° are labeled accordingly. Tissues are assigned one of three shades: dark (low-conductivity tissues, including bone and lung), medium (fat, also a low-conductivity tissue), and bright (high conductivity tissues, including skin, muscle, heart, aorta, blood, tendon, etc.). The location of the coil is shown with white dots. Note that the left-right convention used in radiology is used here: the model's "right" side is on the viewer's left. This is the opposite of the convention used by Wen et al. (11).

Table 1
Normalization Factor V, SAR Levels, Absorbed Power, and SNR at Center of Heart for Whole-Body Model With a Surface Coil (for 3 msec Rectangular Pulse Producing 90° Flip at Center of Heart)

Frequency (MHz)	V	$SAR_{3ms/90°}$ (W/kg) Max. one-cm^3	$SAR_{3ms/90°}$ (W/kg) Average	V^2P_{abs} (W)	Relative SNR
64	77.78	15.24	0.1349	12.91	1.000
125	158.3	58.41	0.4853	45.88	1.946
175	177.4	105.9	0.8883	83.65	2.713
260	378.3	309.8	2.731	200.6	3.895
345	533.8	774.0	6.130	557.0	5.021

Edelstein et al. (2) measured "intrinsic" SNR (ISNR) in the human head and in the human torso at several frequencies up to 64 MHz using linearly-driven volume coils. The results appeared to fall approximately along a straight line that intersected the origin. This agrees very well with calculations presented here for SNR in the torso using a surface coil at frequencies through 345 MHz (Fig. 6) at a location near the center of the heart. Experiments at frequencies of 64 MHz and below, however, are not necessarily good indicators of behavior much above 64 MHz because of the rapidly increasing complexity of the electromagnetic field spatial distribution at such frequencies (Fig. 4).

Both experiment (11) and the calculated results presented here suggest that at frequencies up to 175 MHz, SNR at the center of the heart should increase at a nearly linear rate in experiments using a surface coil near the chest. Our calculations indicate that at the center of the heart this nearly linear increase in SNR may continue to 345 MHz, but it is also important to examine the trend in SNR at locations other than what we have chosen as the center of the heart. At locations 2 cm anterior (location A), posterior (location P), left (reader's right: location L), and right (reader's left: location R) compared to the point at the center (location C), which is shown in Fig. 4 and used for all results presented up to now, the trend in SNR is shown

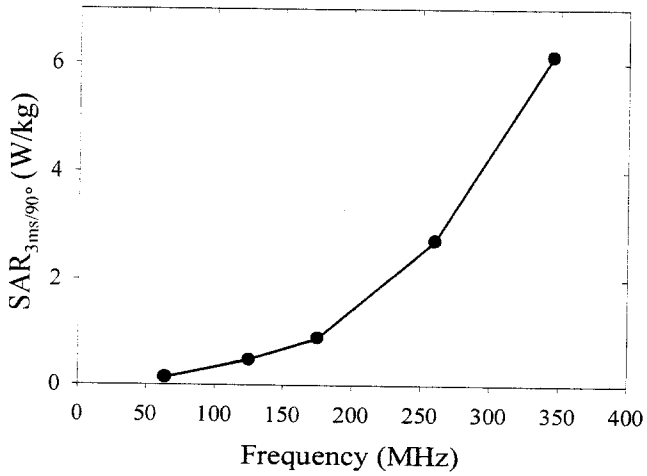

FIG. 5. Line plot of whole-body average $SAR_{3msec/90°}$ as a function of B_1 frequency.

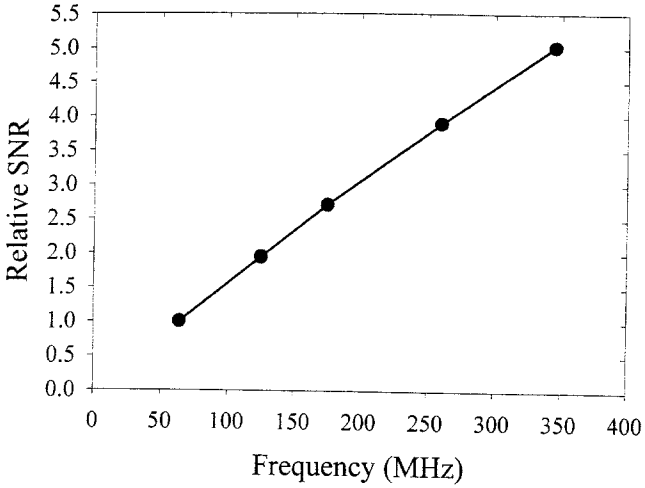

FIG. 6. Line plot of relative SNR as a function of B_1 frequency. Values are normalized to that at 64 MHz. A straight line passed through the two lowest-frequency points and extended towards the origin will very nearly pass through the origin. This suggests good agreement with theory and experiment at low frequencies (1–3).

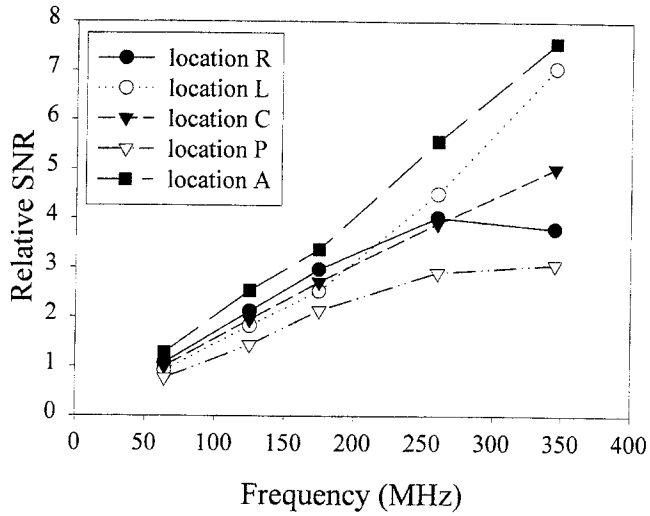

FIG. 8. Line plot of relative SNR at several locations as a function of B_1 frequency when the flip angle is 90° at each respective location.

in Fig. 7 for the 90° pulse defined at location C, and in Fig. 8 for the 90° pulse defined at each respective location. Clearly, at frequencies much above 175 MHz the trend in SNR is very dependent on location due to the changing RF field distribution. Up to about 175 MHz, the SNR increases at an approximately linear rate at each location (Figs. 7 and 8). If the excitation pulse is defined such that the flip angle is 90° at location C, as the RF field distribution becomes more complex with increasing frequency (Fig. 4) the flip angle at neighboring locations will get farther from 90° and the SNR at these locations will become lower than that at location C (Fig. 7). If we calculate SNR as if the flip angle is 90° at each location for its respective data points so that

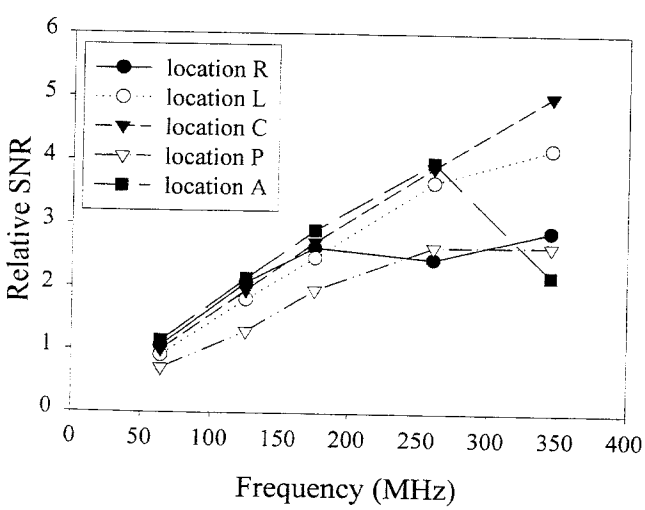

FIG. 7. Line plot of relative SNR at several locations as a function of B_1 frequency when the flip angle is 90° at location C. Locations are 2 cm anterior (location A), posterior (location P), left (reader's right: location L), and right (location R) compared to the point at the center (location C), which is shown in Fig. 4 and was used as the reference for results presented in Figs. 3–6 and Tables 1–2.

SNR is maximized at each location, we see that above 175 MHz the rate of increase (slope) may increase (locations A and L) or decrease (locations P and R) depending on how the RF field pattern changes with frequency (Fig. 8). A similar range of SNR behavior with frequency has been predicted for a body-sized phantom with an elliptical cross-section depending on material properties (4), for a spherical sample excited by a surface coil depending on sample size (8,9), and for a simple axis-symmetric model of the chest depending on model complexity (7).

Methods of assessing SAR in experiment generally rely on measurements of temperature made in homogeneous samples, or on assumptions about what the quality factor of the loaded and empty coil can reveal about the percent of applied power absorbed in the sample (23). While these methods may give a good estimate of the average SAR in a patient, they tell nothing about the distribution of the SAR or the magnitude of the maximum local SAR in a patient. The International Electrotechnical Commission (IEC) has suggested limits on average SAR in the head, average SAR in the body, and SAR in any 1-g region (24). The present limits for the normal operating mode are 1.5 W/kg over any 15 min for whole-body SAR, 3 W/kg averaged over any 10 min for average SAR over the head, and 8 W/kg in any gram of tissue in the head or torso (12 W/kg in any gram of tissue in the extremities) over any 5 min. With methods published previously (25) and the calculated $SAR_{3msec/90°}$ values in Table 1, it is possible to estimate the imaging parameters necessary to avoid exceeding the IEC limits in a number of possible experiments. The SAR levels induced during a pulse with flip angle α and duration τ would be:

$$SAR_{\tau/\alpha} = r\left(\frac{3ms}{\tau}\right)^2\left(\frac{\alpha}{90°}\right)^2 SAR_{3ms/90°} \qquad [5]$$

where r is a factor determined by the type of pulse used, calculated as a power ratio of the given pulse to a rectangular pulse with the same α and τ. If a rectangular pulse is

used, $r = 1.0$. If a Gaussian pulse is used, τ is defined as the full-width half-maximum of the Gaussian, and $r = 0.67$ (23). If a sinc pulse is used, τ is defined as the width of the central lobe at the zero crossings, and $r = 2.0$ (23). The SAR levels of a given pulse sequence will be equal to the sum of the energy absorbed from the pulses during the total image acquisition time divided by the total acquisition time. This can be written in general as:

$$\mathrm{SAR} = \frac{\sum_{n=1}^{N} (\mathrm{SAR}_{\tau n/\alpha n} \times \tau n)}{\mathrm{TT}} \qquad [6]$$

where αn and τn are the flip angle and pulse duration of the nth pulse in a sequence of N RF pulses, and TT is the total time necessary to acquire the image. Assuming the same N RF pulses are used in each repetition of a pulse sequence so that SAR over the total imaging time TT is equal to that over TR, we can calculate the minimum permissible TR to avoid exceeding some limit in SAR ($\mathrm{SAR}_{\mathrm{lim}}$) as:

$$\mathrm{TR} \geq \frac{\sum_{n=1}^{N} (\mathrm{SAR}_{\tau n/\alpha n} \times \tau n)}{\mathrm{SAR}_{\mathrm{lim}}} \qquad [7]$$

where $\mathrm{SAR}_{\tau n/\alpha n}$ can be calculated for any standard pulse type of duration τn and flip angle αn from the $\mathrm{SAR}_{3\mathrm{msec}/90°}$ values in Table 1 with Eq. [5]. Since for soft tissues (where conductivity and SAR are typically highest) the material density is very near 1 g/cm^3, the maximum SAR in one cm^3 will be very close to that for 1 g. The IEC normal operating mode limit for 1-g SAR in the body is greater than the limit for average SAR in the body by a factor of about 5.3. In Table 1 at every frequency the maximum 1-cm^3 SAR is greater than the whole-body average SAR by a factor of >100. Thus, in every case calculated here the local SAR level is the limiting factor for imaging parameters.

Assuming that only rectangular 90° and 180° pulses (flip angle defined at center of heart) are used, that 90° pulses have $\tau = 3$ msec and 180° degree pulses have $\tau = 6$ msec, it is possible to calculate the minimum allowable TR for a number of imaging sequences using 8 W/kg as $\mathrm{SAR}_{\mathrm{lim}}$ and the maximum 1-cm^3 SAR levels in Table 1 for $\mathrm{SAR}_{3\mathrm{msec}/90°}$. The minimum allowable TR for several pulse sequences at several frequencies with these assumptions for a surface coil near a chest is given in Table 2. The values in Table 2 could be multiplied by appropriate factors to account for other pulse types and durations that might be used. These numerical results are technically only valid for the model and coil arrangement presented here. Nonetheless, these numbers may serve as a rough guide to what types of experiments should be possible at various frequencies with a large, muscular male subject and a surface coil on the chest. It appears that in experiments other than echo-planar imaging (EPI), gradient echo (GE), and spin echo (SE) sequences at 175 MHz and below, and perhaps the 8-echo rapid acquisition with relaxation enhancement (RARE8) sequence at 64 MHz, SAR will be a consideration.

Table 2
Minimum Allowable TR for Surface Coil on Chest With Several Pulse Sequences at Several Frequencies Assuming Only 3 msec Rectangular 90° and 6 msec Rectangular 180° Pulses Are Used

Frequency (MHz)	Minimum allowable TR (msec)				
	EPI	GE	SE	RARE 8	RARE 32
64	5.715	5.715	17.14	97.16	371.5
125	21.90	21.90	65.70	372.3	1242
175	39.71	39.71	119.3	675.1	2581
260	116.2	116.2	348.6	1975	7553
345	290.2	290.2	870.6	4933	18863

In these calculations the location of the maximum SAR in 1 g (cubic cm) of tissue occurs at nearly the same location at each frequency. This location is in the right medial portion of the pectoral muscle near the superior end of the sternum. This is interesting because this location is not the closest to the coil or to its voltage sources. We speculate that the SAR is highest here in this individual because the largest conductive bodies near the coil are the pectoral muscles, and since the thickness of these muscles diminishes as they approach the sternum, the current density will be increased in this region. In a subject with less pronounced pectoral muscles, this maximum might occur elsewhere. This emphasizes the importance of specific subject anatomy in determining the location of greatest SAR.

The FDA and IEC limits on SAR levels may change with time, but with the data and equations presented here it should be possible to estimate what imaging parameters are necessary to avoid exceeding future limits on SAR for coils and human geometries such as those modeled in this work.

CONCLUSIONS

Until recently, computational limitations have made calculations of SNR and SAR with increasing B_1 frequency impossible except in simple geometries. Here we have used numerical methods to predict SNR and SAR for a large, muscular male with a surface coil against his chest. Our calculations suggest that in this particular case, at frequencies above 175 MHz, SNR may increase or decrease with increasing B_1 frequency depending on the location and definition of the excitation pulse. This prediction is very dependent on the sample geometry and B_1 coil, as similar calculations for a head in a birdcage coil indicate that SAR and SNR will not pose problems at frequencies up to 8T (5). Clearly, there are major limitations and assumptions in these calculations. T_1, T_2, static field inhomogeneity, and a host of other factors are not considered. Still, in looking for fundamental relationships due to RF field behavior, the methods used here are well understood and generally accepted (2–9).

ACKNOWLEDGMENTS

We are grateful to Belinda G. Collins, M.D., Ph.D., and Timothy J. Mosher, M.D., for their expert advice in segmenting images for the production of the head model used

here, and to Harvey E. Smith, A.B., for his assistance in segmentation. We have benefited greatly from enlightening discussions and correspondence with Dr. David I. Hoult, including rigorous proofs of the necessary equations for calculating detected signal.

REFERENCES

1. Hoult DI, Lauterbur PC. The sensitivity of the zeugmatographic experiment involving human samples. J Magn Reson 1979;34:425–433.
2. Edelstein WA, Glover GH, Hardy CJ, Redington RW. The intrinsic signal-to-noise ratio in NMR imaging. Magn Reson Med 1986;3:604–618.
3. Hoult DI, Chen C-N, Sank VJ. The field dependence of NMR imaging: ii. arguments concerning an optimal field strength. Magn Reson Med 1986;3:730–746.
4. Ocali O, Atalar E. Ultimate intrinsic signal-to-noise ratio in MRI. Magn Reson Imaging 1998;39:462–473.
5. Collins CM, Smith MB. Calculated B_1 homogeneity, SNR, and SAR vs. frequency for an idealized quadrature birdcage coil. In: Proceedings of the7th Annual Meeting of ISMRM, Philadelphia, 1999. p 417.
6. Collins CM, Smith MB. Calculated SNR and SAR vs. frequency for a surface coil on the human chest. In: Proceedings of the7th Annual Meeting of ISMRM, Philadelphia, 1999. p 418.
7. Singerman RW, Denison TJ, Wen H, Balaban RS. Simulation of B_1 field distribution and intrinsic signal-to-noise in cardiac MRI as a function of static magnetic field. J Magn Reson 1997;125:72–83.
8. Carlson JW. Radiofrequency field propogation in conductive NMR samples. J Magn Reson 1988;78:563–573.
9. Keltner JR, Carlson JW, Roos MS, Wong STS, Wong TL, Buddinger TF. Electromagnetic fields of surface coil *in vivo* NMR at high frequencies. Magn Reson Med 1991;22:467–480.
10. Hoult DI. Sensitivity and power deposition in a high-field imaging experiment. J Magn Reson Imaging 2000;12:46–67.
11. Wen H, Denison TJ, Singerman RW, Balaban RS. The intrinsic signal-to-noise ratio in human cardiac imaging at 1.5, 3, and 4 T. J Magn Reson 1997;125:65–71.
12. Yee KS. Numerical solution of initial boundary value problems involving Maxwell's equations in isotropic media. IEEE Trans Ant Propag 1966;14:302–307.
13. Kunz KS, Luebbers RJ. The finite difference time domain method for electromagnetics. Boca Raton: CRC Press; 1993.
14. Collins CM, Smith MB. FDTD grid resolution and accuracy in SAR calculations for MRI. In: Proceedings of the 7th Annual Meeting of ISMRM, Philadelphia, 1999. p 2051.
15. Jin JM, Chen J, Chew WC, Gan H, Magin RL, Dimbylow PJ. Computation of electromagnetic fields for high-frequency magnetic resonance imaging applications. Phys Med Biol 1996;41:2719–2738.
16. Wlodzimierz E, Gos T. Density of trunk tissues of young and medium age people. J Biomech 1990;23:945–947.
17. Huang HK, Wu SC. The evaluation of mass densities of the human body in vivo from CT scans. Comput Biol Med 1976;6:337–343.
18. Cho ZH, Tsai CM, Wilson G. Study of contrast and modulation mechanisms in x-ray/photon transverse axial transmission tomography. Phys Med Biol 1975;20:879–889.
19. Clauser CE, McConville JT, and Young JW. Weight, volume, and center of mass of segments of the human body. Aerospace medical research laboratory, Wright-Patterson Air Force Base, Ohio: AMRL-TR-69-70; 1969.
20. Gabriel C. Compilation of the dielectric properties of body tissues at RF and microwave frequencies. Air Force materiel command, Brooks Air Force Base, Texas: AL/OE-TR-1996-0037; 1996.
21. Hoult DI. The principle of reciprocity in signal strength calculations—a mathematical guide. Concepts Magn Reson 2000;4:173–187.
22. Bendall RM. Surface coil technology. In: Partain CL, Price RR, Patton JA, Kulkarni MV, James Jr AE, editors. Magnetic resonance imaging. Philadelphia: WB Saunders; 1988. p 1201–1268.
23. Bottomley PA, Redington RW, Edelstein WA, Schenck JF. Estimating radiofrequency power deposition in body NMR imaging. Magn Reson Med 1985;2:336–349.
24. International Electrotechnical Commission. Medical electrical equipment, part 2: particular requirements for the safety of magnetic resonance equipment for medical diagnosis. IEC 601-2-33; 1995.
25. Collins CM, Li S, Smith MB. SAR and B_1 field distributions in a heterogeneous human head model within a birdcage coil. Magn Reson Med 1998;40:847–856.

Measurements and FDTD Computations of the IEEE SCC 34 Spherical Bowl and Dipole Antenna

Martin Siegbahn and Christer Törnevik
Ericsson Radio Systems AB, S-164 80 Stockholm, Sweden
Phone: +46 8 7570811/7641235, Fax: +46 8 58531480
E-mail: martin.siegbahn@era-t.ericsson.se,
christer.tornevik@era-t.ericsson.se

Summary

SAR and feedpoint impedance have been measured and FDTD computed for a spherical bowl and a λ/2 dipole at 835 MHz according to procedures outlined by IEEE SCC 34, WG 1. Good agreement between measurement and FDTD computation was found both for the SAR distribution in the bowl and for the antenna feedpoint impedance.

1 Introduction

In order to evaluate the ability of the current state-of-the-art dosimetric nearfield measurement systems and computational tools to assess and predictate the electromagnetic fields close to low power radio transmitters the IEEE SCC 34 working group 1 has specified a number of so called canonical problems for benchmark testing. One of the problems involves a spherical glass bowl filled with brain simulating liquid and a wire dipole antenna which is placed below the bowl for inducing EM fields in the liquid [1]. The test consists of measurements or computations of the antenna feedpoint impedance as well as mapping of the specific absorption rate (SAR) in the liquid. This report describes the performed measurements and FDTD computations and the obtained results for this test at the EMF laboratory at Ericsson Radio Systems AB in Stockholm during May and June1998.

2 Measurements

The measurement procedures specify measurements of the SAR distribution from a λ/2 wire dipole at 835 MHz in a spherical pyrex glass bowl filled with brain simulating liquid and the feedpoint impedance of this antenna when it is placed both symmetrically and asymmetrically below the bowl as shown in Fig. 1. The bowl has an outer diameter of 224 ± 0.5 mm and a glass thickness 5 ± 0.5 mm and the dipole has an overall length equal to 168 mm and a coaxial wire thickness of 3.6 mm. The dimensions of the dipole [2] are shown in Fig. 2. The opening in the spherical bowl is 170 mm in diameter (D_2) and was chosen as to disturb the EM field distribution in the southern hemisphere as little as possible [1]. The liquid level was equal to 150 mm during all measurements.

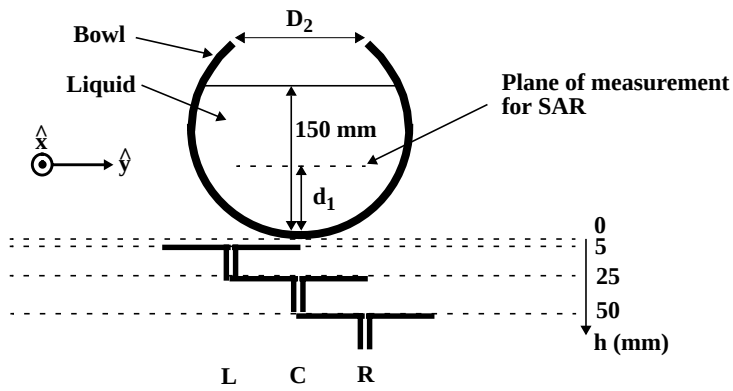

Figure 1. Three of the eleven different antenna positions below the spherical bowl. The separation between the bowl and the antenna is measured from the outer surface of both structures.

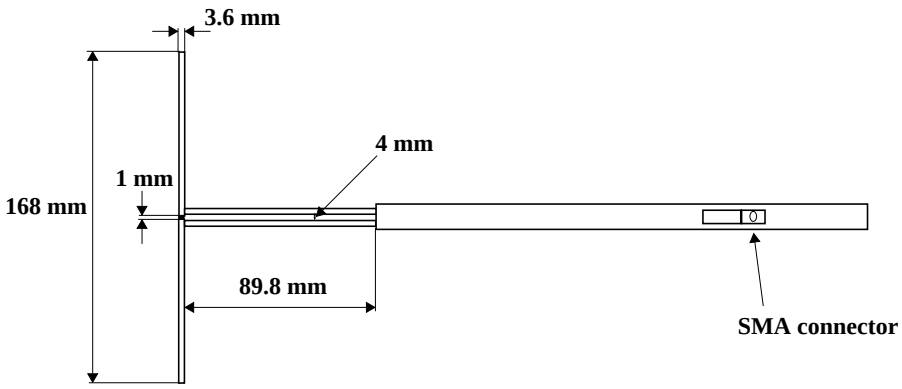

Figure 2. The 835 MHz λ/2 dipole used in the measurements. The antenna was manufactured by Schmid & Partner Engineering AG with the model number D835V2 (S/N:401).

The measurement protocol states that the spherical bowl is filled with brain simulating liquid with a relative permittivity equal to 44.0 and a conductivity of 0.90 S/m. A recipe for mixing such a liquid was found by modifying a recipe giving similar parameters [3]; 41.5% water, 56.0% sugar, 1.4% salt, 1.0% HEC and 0.1% Preventol-7. The electrical parameters for this liquid were measured with a HP87050B dielectric probe kit and found to be at 835 MHz ε_r=42.9±5% and σ=0.90±10% S/m [4].

Fig. 3 shows the laboratory setup for the measurements. A metal tripod holds the antenna and in order to properly position the antenna and the bowl a special fiberglass table with a 200 mm hole in the upper surface had to be fabricated. The distance between the antenna and the bowl was determined by use of a vernier calliper and the overall alignment by a water level.

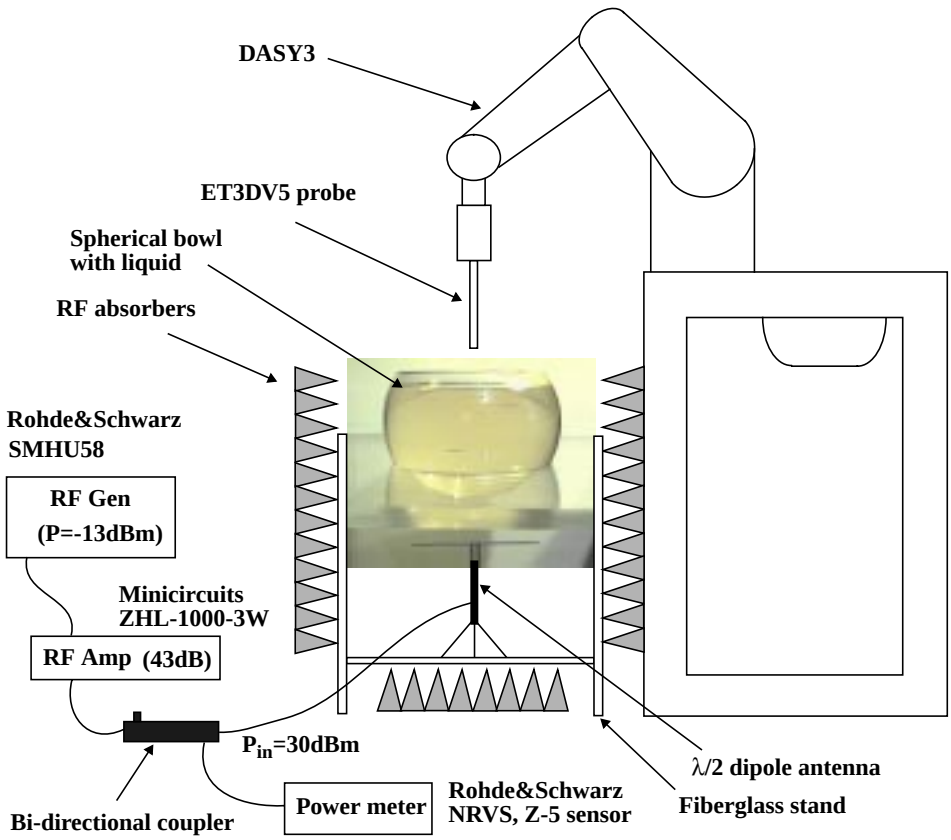

Figure 3. The laboratory setup for the IEEE SCC 34 spherical bowl and dipole experiment.

The dosimetric nearfield measurement system used for the SAR measurements was the DASY3 [5] from Schmid & Partner Engineering AG with the isotropic E-field probe ET3DV5 [6]. The probe correction factor used for all SAR measurements in the bowl was equal to 6.1.

The impedance of the 835 MHz λ/2 dipole was measured with a HP8752C network analyzer when the antenna was placed in all eleven different positions with respect to the bowl; as centered at distances (denoted h) 5, 25 and 50 mm below the outer south pole and translated on both sides so that alternatively one of the antenna tips will be placed under the south pole at the same distances plus 0 mm. The SAR in the bowl was measured at the axis of symmetry for five of the positions; in the centered position with h=5, 25 and 50 mm and left/right translated with h=0 mm. Complete SAR scanning in horizontal planes at height d_1 from the inner south pole was performed for the centered position at h=5 mm and left/right position at h=0 mm. The impedance measurements were conducted five times giving eleven values for each series and the SAR measurements were repeated three times. The complete SAR scanning was performed once for every measurement series but each axis of symmetry measurement was repeated five times in sequence in order to give reliable results.

3 FDTD computations

The spherical bowl and the dipole were modeled in a cubical FDTD grid [7] with grid step equal to 2.5 mm, as shown in Fig. 4 and Fig. 5. This grid step was chosen as suitable for computing distances 5, 25 and 50 mm between the bowl and the antenna but also giving moderate modeling errors for the dimensions of both structures. Obviously, in order to have a symmetrical antenna, the length of the antenna model is always an odd number of cells and therefore the diameter of the bowl also has to be an odd number of cells if the antenna is to be placed in a true centered position below the bowl. This requires though that the antenna is modeled as a bar of cells rather than by a thin filament of FDTD components if the models are to be symmetrical also in the plane perpendicular to the antenna axis. However, when modeling the case with a asymmetrically positioned antenna the tip of the dipole is not possible to placed directly under the outer south pole but it will be a half grid step offset from this position.

The FDTD components in the glass-liquid boundary, i.e. on the inside of the bowl, were computed with the material parameters set equal to those for the liquid since the pyrex glass has a zero conductivity. In the 2.5 mm grid, the bowl has an outer diameter of 89 cells, i.e. 222.5 mm, and an inner diameter of 85 cells, i.e. 212.5 mm. The antenna is represented by two bars each 33 cells long with a one by one cell cross section giving an overall length, including the voltage source gap, of 67 cells or 167.5 mm.

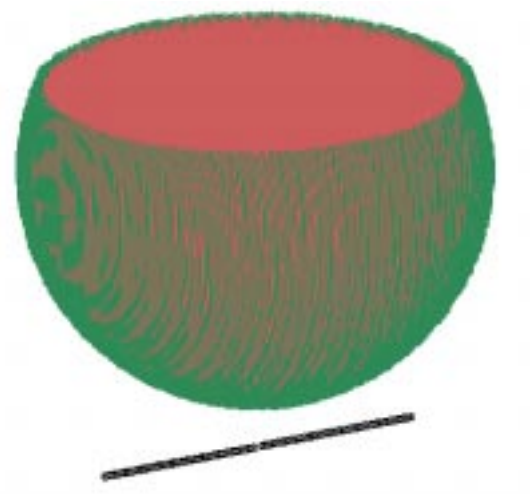

Figure 4. The FDTD models of the spherical bowl and the λ/2 dipole. The dipole is placed as centered 25 mm below the outer south pole of the bowl.

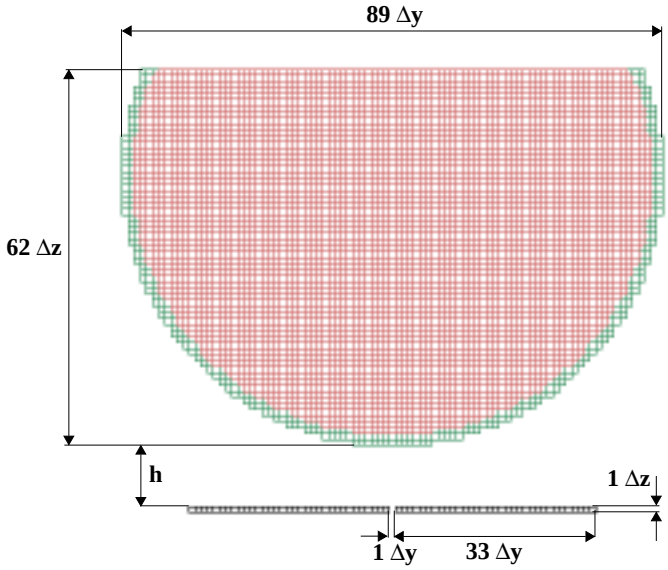

Figure 5. The dimensions of the FDTD models. The separation h between the bowl and the dipole, was 2, 10 and 20 cells corresponding to distances 5, 25 and 50 mm.

The bowl and the halfwave dipole were placed in the FDTD grid with a minimum distance to the Liao boundary of λ/3 giving a total computational volume of 165x165x165 cells for the computations with the dipole in a centered position and 165x190x165 cells for the case when it was placed asymmetrically. The memory requirements for these grids were 127 and 146 Mbyte respectively in the XFDTD version 4.04 code [8] and on the 300 MHz Sun Ultra-30 computer the computational time was about 5h 15min.

4 Measurement and FDTD Results

4.1 Antenna feedpoint impedance

Table 1 summarizes the obtained measured and FDTD computed feedpoint impedance of the half-wave dipole antenna when it was positioned in the different positions. Note, the FDTD data for the left translated antenna is only a copy of the right side data since computations of this case will give close to identical values, which is of course due to the symmetry of the applied models.

Position	h(mm)	Measured Re(Z), mean value (Ω)	Measured Im(Z), mean value (Ω)	FDTD Re(Z) (Ω)	FDTD Im (Z) (Ω)
Centered	5	49.7	-4.6	48.9	-2.8
Centered	25	53.9	14.8	48.9	18.5
Centered	50	74.9	23.4	66.0	29.6
Right	0	104.6	91.4	178.6	159.2
Right	5	82.0	45.5	90.5	44.2
Right	25	75.1	24.6	75.1	23.8
Right	50	84.2	20.6	78.8	22.3
Left	0	105.1	89.9	178.6	159.2
Left	5	82.8	43.6	90.5	44.1
Left	25	76.6	22.7	75.1	23.8
Left	50	85.8	18.9	78.8	22.3

Table 1 The measured and FDTD computed feedpoint impedance for the λ/2 dipole at 835MHz.

The maximum differences between the measured right side and the left side values are 1.6 Ω for the resistance and 2.0 Ω for the reactance. The standard deviation for the measured resistance ranges from 0.4 to 12.9 Ω and for the measured reactance 0.4 to 2.8 Ω. The maximum difference between the measured mean and the FDTD computed impedance for the centered position is of the order 6 to 9 Ω.

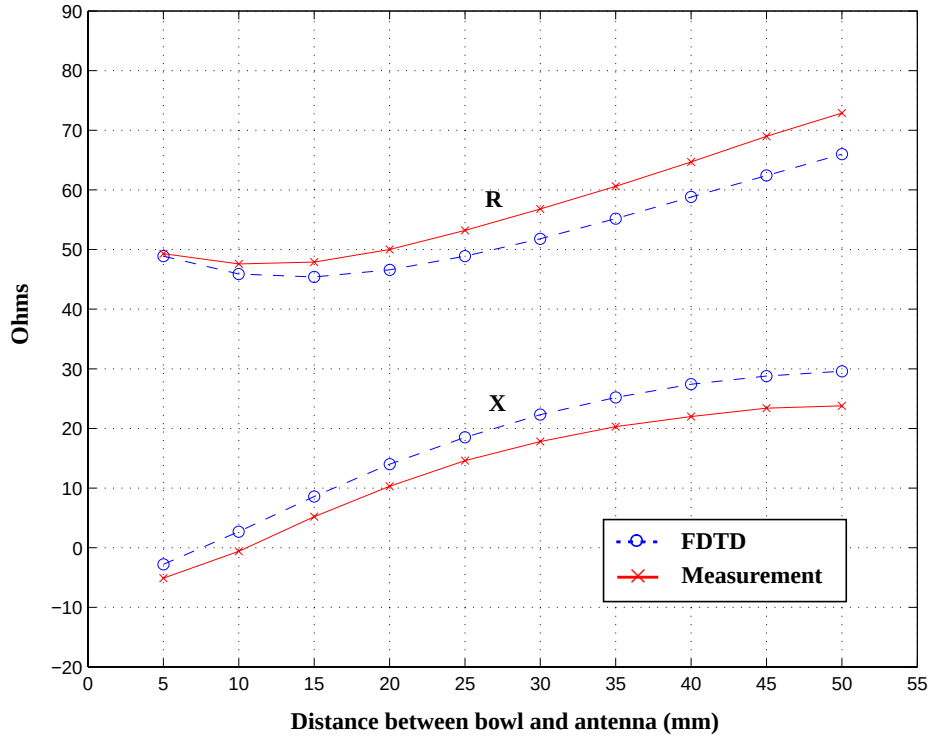

Figure 6. FDTD computed vs. measured dipole feedpoint impedance for centered antenna position. The measured impedance displayed are only based on one series of values.

An additional series of impedance measurements were performed for the case when the dipole was placed symmetrically below the bowl. The impedance was measured for distances h=5 to 55 mm in 5 mm steps in order to investigate the overall antenna-bowl separation dependence of the feedpoint impedance. Corresponding FDTD computations were also carried out and the results are shown in Fig. 6. The agreement between measurement and FDTD calculation is very good and the mean difference is only about 4 Ω for both the resistance and the reactance. Obviously, the selected FDTD models seem suitable for computing the feedpoint impedance even though they are, in certain aspects, somewhat coarse.

4.2 SAR results

In order to properly compare the measured and the FDTD computed SAR distributions in the bowl, the FDTD values had to be calculated by averaging over several computational cells and E-field components [9]. All SAR values were normalized to 1W of radiated power.

4.2.1 SAR on the axis of symmetry

The measured and the FDTD computed local SAR on the axis of symmetry in the spherical bowl when the antenna was placed symmetrically below it is shown in Fig. 7. The agreement between measurement and FDTD computation is very good for all distances between the bowl and the antenna. The peak local SAR is, of course, located at the inner surface of the bowl and falls off quite rapidly with increasing height/distance from the inner surface The measured SAR decreases somewhat faster though than the FDTD data close to the inner south pole. However, small deviations in probe positioning in this area lead to large variations in measured SAR which is shown by the standard deviation for these measurement points, about 1.7 W/kg for the distance 2.7 mm when h was equal to 5mm.

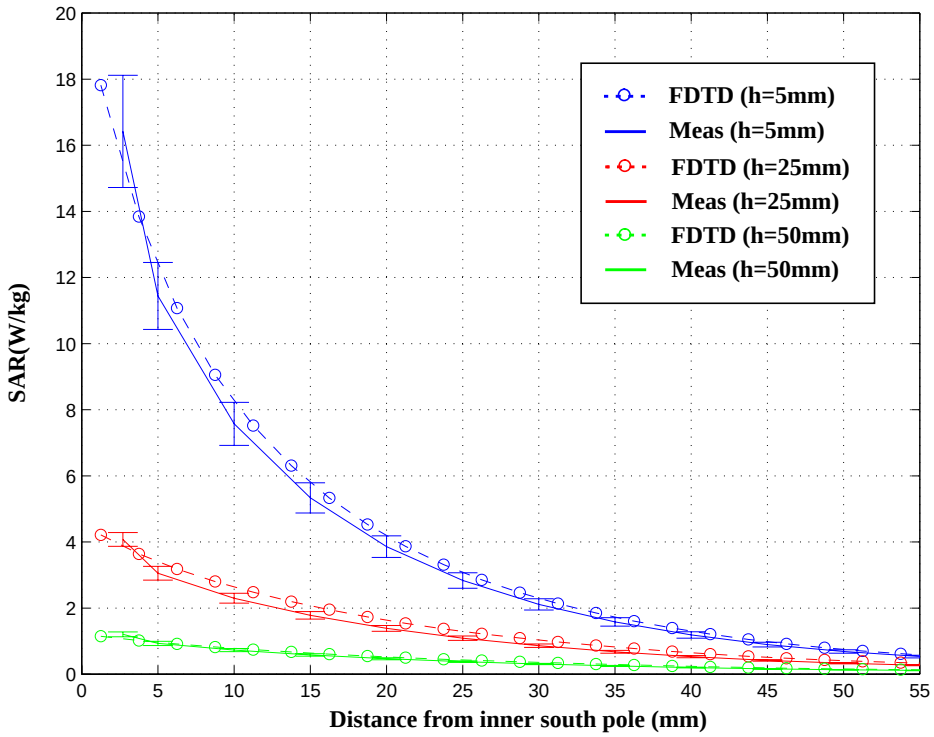

Figure 7. FDTD computed vs. measured SAR on the axis of symmetry for the spherical bowl. The dipole was placed as centered 5, 25 and 50 mm below the outer south pole.

The SAR decrease due to increased separation between the bowl and the dipole antenna is also clearly understandable and an increase in h from 5 mm to 50 mm decreases the maximum SAR almost by a factor of 10 both in the measurements and in the FDTD computations. The mean difference between the measurement and the FDTD data is 0.2 W/kg for h=5 mm, 0.1 W/kg for h=25 mm and only 0.03 W/kg for h=50mm.

For the cases when the dipole antenna was translated to the left and right side of the bowl the measured and the FDTD computed local SAR on the axis of symmetry for the bowl are shown in Fig. 8. The agreement between measurement and computation is not as good as when the dipole antenna was placed in a centered position. Here, the FDTD computed SAR close to the surface is lower than the measured value. The maximum difference between the two data sets is for the left translated position about 5.4 W/kg close to the inner surface but the overall mean difference is only of the order 0.3 W/kg. For the right translated case the corresponding differences are 4.7 W/kg and 0.3 W/kg. However, the agreement between the two measurement data sets is rather good though which indicates good positioning and alignment of the laboratory setup.

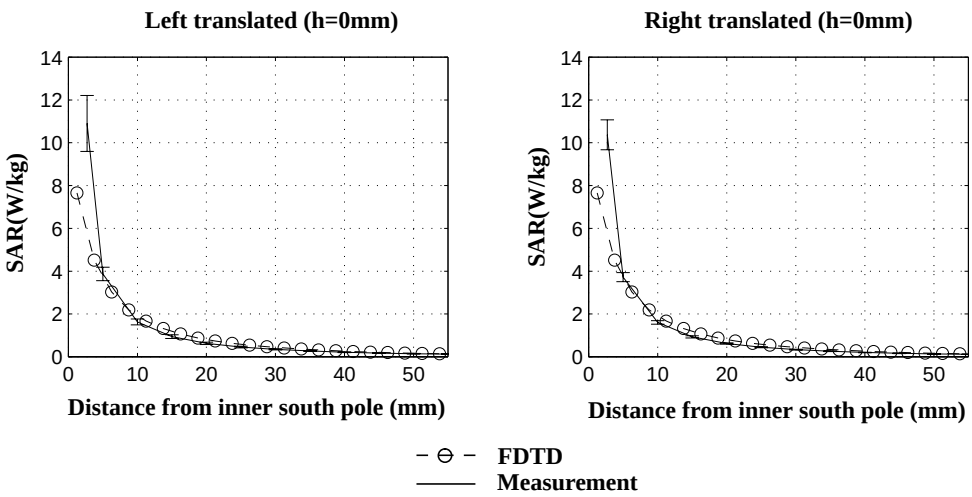

Figure 8. The measured and the FDTD computed SAR on the axis of symmetry for the spherical bowl. The half-wave dipole antenna was placed 0 mm below the outer south pole and translated to the left and right side.

4.2.2 SAR in horizontal planes at heights d_1 above the inner south pole

Local SAR measured and computed in horizontal planes at heights d_1=30 mm and d_1=50 mm from the inner south pole for the symmetrically positioned antenna at h=5 mm are shown in Fig. 9 and 10. The agreement between the measured and the FDTD computed SAR is quite good both in terms of absolute value and shape. The mean difference is only of the order 0.1 W/kg for both planes. At the height d_1=30 mm the axis of the antenna is clearly visible as a ridge in the SAR distribution along the y-axis but at d_1=50 mm the distribution is more or less symmetrical around the maximum value located at the center of the plane.

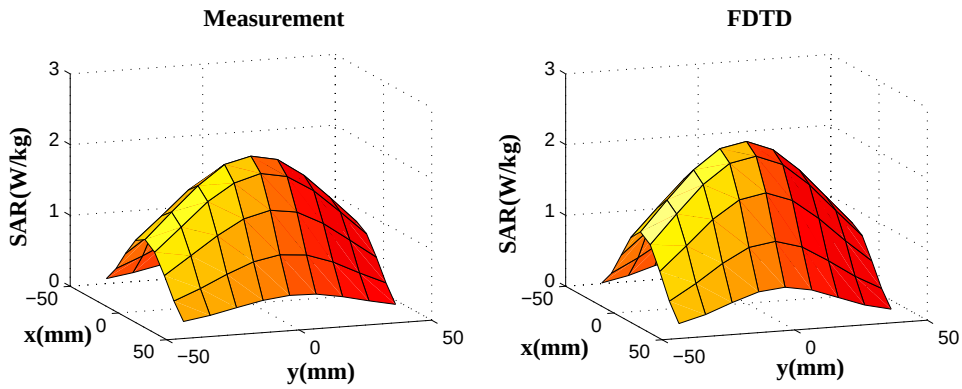

Figure 9. Local SAR in the plane d_1=30 mm for the center antenna position at h=5 mm. The maximum and the mean differences between the measurement and the FDTD computation are 0.3 W/kg and 0.1 W/kg.

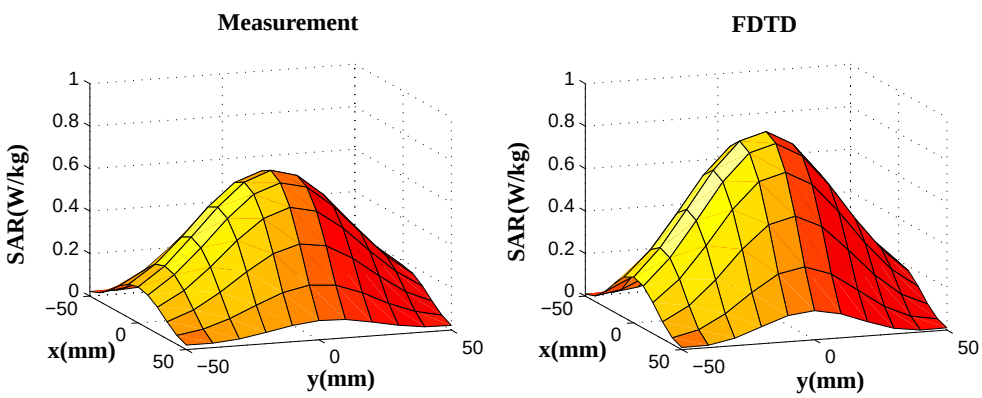

Figure 10. Local SAR in the plane d_1=50 mm for the center antenna position at h=5 mm. The maximum and the mean differences between the measurement and the FDTD results are 0.2 W/kg and 0.06 W/kg.

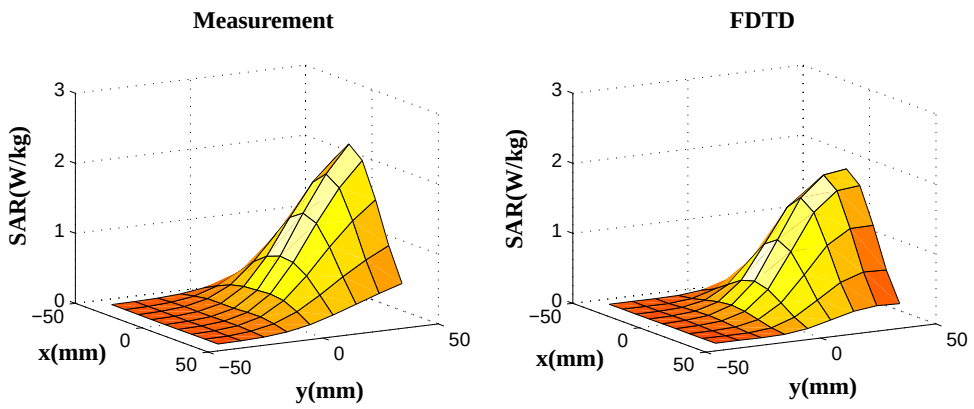

Figure 11. Local SAR in the plane d_1=50 mm for the right translated antenna position at h=0 mm. The maximum and the mean differences between the measurement and the FDTD computation are 0.4 W/kg and 0.1 W/kg.

In Fig. 11, the SAR distribution at d_1=30 mm for the right translated antenna position are shown. The maximum value of this distribution is located at the right side of the plane and here there are some differences between measurement and FDTD computation. This is probably due to the fact that the tip of the antenna in the FDTD model is not possible to perfectly position at the outer south pole but is located half a grid step to the right of the pole.

5 Conclusions and Future work

Measurements and corresponding FDTD computations have been performed for the IEEE SCC 34 spherical bowl and dipole benchmark test with good agreement in the obtained results both in terms of the antenna feedpoint impedance and the SAR distribution in the bowl. The mean difference between measured and FDTD calculated impedance was found to be around 6-9 Ω and the mean difference between the measured and the FDTD computed SAR in the bowl was of the order 0.05-0.4 W/kg. However, the uncertainties and errors affecting the measurement and the FDTD results both in terms of SAR and impedance have not yet been finally calculated but will be included and described in the next revision of this document.

6 References

[1] IEEE SCC 34, WG 1, "Spherical Phantom Experimental Protocol", 2nd Draft, 1998.

[2] Thomas Schmid and Katja Pokovic, "FCC Benchmark Dipole B", Swiss Federal Institute of Technology Zurich, 8096 Zurich, Switzerland.

[3] G. Hartsgrove, A. Kraszewski and A. Surowiec, "Simulated biological materials for electromagnetic radiation absorption studies", *Bioelectromagnetics*, vol. 8, pp. 29-36, 1997.

[4] Hewlett-Packard Company, "HP85070B Dielectric Probe Kit User's manual", HP part number 85070-90009, 1993.

[5] Thomas Schmid, Oliver Egger, Niels Kuster, "Automated E-field scanning system for dosimetric assessments", *IEEE transactions on Microwave Theory and Techniques*, vol. 44, pp. 105-113, January 1996.

[6] Klaus Meier, Michael Burkhardt, Thomas Schmid and Niels Kuster, "Broadband calibration of E-field probes in lossy media", *IEEE transactions on Microwave Theory and Techniques*, vol. 44, no. 10, pp. 1954-1962, October 1996.

[7] Karl S. Kunz, Raymond J. Luebbers, "The Finite Difference Time Domain Method for Electromagnetics", CRC Press, 1993.

[8] Remcom Inc., "User's Manual for XFDTD the X-Window Finite Difference Time Domain Graphical User Interface for Electromagnetic Calculations", Version 4.04, October 1997.

[9] K. Caputa, M. Okoniewski and Maria A. Stuchly, "An Algorithm for Computations of the Power Deposition in Human Tissue with the FDTD Method", Proceedings of the USNC/URSI National Radio Science Meeting 1998, Atlanta, Georgia, U.S, June 21-26 1998, pp. 197.

CALCULATION OF ELECTRIC FIELDS AND CURRENTS INDUCED IN A MILLIMETER-RESOLUTION HUMAN MODEL AT 60 Hz USING THE FDTD METHOD WITH A NOVEL TIME-TO-FREQUENCY-DOMAIN CONVERSION

Cynthia M. Furse and O. P. Gandhi
Department of Electrical Engineering
University of Utah
Salt Lake City, Utah 84112

Abstract

The finite-difference time-domain (FDTD) method has previously been used to calculate induced currents in anatomically based models of the human body at frequencies ranging from 20 to 915 MHz and resolutions down to 1.31 cm [1]. Calculations at lower frequencies and higher resolutions have been precluded by the huge number of time steps which would be needed to run these simulations in the traditional way. This paper describes a new method used to overcome this problem and calculate the induced currents in a MRI-based 6-mm-resolution human model at 60 Hz. A new algorithm based on solving two equations with two unknowns is used for calculating magnitude and phase from the CW FDTD simulation. This allows magnitude and phase calculations to be made as soon as steady-state is reached, which is within a fraction of a cycle. For incident electric fields of 10 kV/m, local induced current densities above 16 mA/m^2 have been calculated in the torso, with even higher values up to 65 mA/m^2 for the legs. These are considerably higher than the 4 or even 10 mA/m^2 that have been suggested in the safety guidelines [10].

Introduction

The finite-difference time-domain method has been used extensively for analyzing steady-state frequency-domain behavior in numerous applications. Specific absorption rate (SAR) [1], radar cross section [2], current distribution [3], and S-parameters [4] are a few of the frequency-domain parameters calculated using the FDTD method. Since FDTD is a time-domain method, some conversion must be made from the time to frequency domains. Traditionally this is done with either a peak detection method or a Fourier transform method. Both of these methods require a large amount of computer time and memory, and require that the simulation be run at least half a cycle after convergence has been reached. For applications such as finding the complete current distribution within the human body, these time-to-frequency-domain calculations require as much memory and more computer time than the FDTD simulation itself. This paper describes an alternative to these traditional time-to-frequency-domain calculations which virtually eliminates the computer time required and can dramatically reduce or eliminate the storage requirements as well.

Novel Two-Equation Two-unknowns Time-to-Frequency-Domain Calculations

At a given location in space we can write

$$A \sin(\omega t_1 + \theta) = q_1$$
$$A \sin(\omega t_2 + \theta) = q_2$$

0-7803-3216-4/96/$5.00 © 1996 IEEE

where A is the amplitude, θ is the phase angle ω (= 2 πf) is the angular frequency. At two times, t_1 and t_2, the values q_1 and q_2 are obtained from the FDTD simulation. Therefore, these equations can be solved for the unknowns, A and θ, to give direct relationships for these values

$$\theta = \tan^{-1} [q_2 \sin(\omega t_1) - q_1 \sin(\omega t_2) + q_1 \cos(\omega t_2) - q_2 \cos(\omega t_1)]$$

$$A = |q_1/\sin(\omega t_1 + \theta|$$

Double precision should be used for accuracy, even if the rest of the FDTD simulation is single precision. The choice of t_1 and t_2 depends on the simulation. For most FDTD simulations, the spatial resolution, Δ_x, is on the order of $\lambda/10$ to $\lambda/100$. For these simulations, t_1 and t_2 can be the last two time steps. For higher resolutions, as t_1 and t_2 become closer in seconds, the values of q_1 and q_2 also become closer and closer, and the roundoff errors become more significant. t_1 and t_2 are taken a few time steps apart (25 was used for this paper) to reduce the roundoff errors. This method provides accuracy similar to the Fourier transform method for both magnitude and phase. An additional source of errors which must be avoided is dc offsets and numerical noise in the time-domain data. Ramped sine excitations known not to cause a dc offset should be used [5]. These excitations have also been shown to reduce numerical noise [6].

This new method provides dramatic savings in computer time and memory over the traditional methods of peak detection or Fourier transformation as shown in Table 1. These savings are obtained because both the peak detection and Fourier transform methods require calculations to be made over the last half-cycle of the simulation, and the two-equation two-unknowns method requires only a single calculation. In addition to the savings from the computation of frequency-domain values, significant savings are also obtained for low-frequency calculations because the simulation does not need to be run for a full cycle past convergence as it must be for peak detection and Fourier transform.

Table 1. Comparison of peak detection, Fourier transform, and the two-equation two-unknowns methods of transforming from time domain to frequency domain methods. The FDTD model is $308 \times 99 \times 67$, cell size is 6 mm, Courant number is 0.5. E_x, E_y, and E_z are converted from time to frequency domain for all cells. Frequency is 10 MHz, number of time steps per cycle is 10,000. The FDTD simulation is run for 10,000 time steps.) Cputime is measured on an HP 755 workstation.

	cpumin	Mwords
FDTD time-domain simulation	2054	18.2
Discrete Fourier Transform	3640	15.1
Peak Detection	2147.1	7.56
Two-equation two-unknowns	2.9	7.56 (disk or RAM)

Millimeter-Resolution Model of the Human Body

In collaboration with Dr. James Lee of the Medical Imaging Laboratory, School of Medicine, and Dr. Mark Nielson of the Department of Biology, University of Utah, a millimeter-resolution model of the human body from the MRI scans of a male volunteer was developed. The resolution is 1.974 mm in the axial plane and 3 mm along the height of the body. The MRI sections were converted into images with defined 30 tissue types whose electrical properties are then specified at the radiation frequency. The tissues are fat, muscle, compact bone and bone marrow, cartilage, skin, brain, nerve, cerebrospinal fluid (CSF) intestine, spleen, pancreas, heart, blood, eye humor, sclera, lens, liver, kidney, lung bladder, stomach, ligament, testicle, spermatic cord, prostate, pineal gland, pituitary gland, and erectile tissue. The pineal gland is suspected of being involved in the bioeffects of power frequency EMFs and has, therefore, been separately identified.

Since it is impossible to run the $1.974 \times 1.974 \times 3$ mm resolution model with the memory sources readily available to us, the voxels were combined to give averaged electrical properties in a $6 \times 6 \times 6$ mm^3 model. Using 5 cells to the second-order Mur absorbing boundaries, and a perfectly conducting ground plane under the feet, the model requires a calculation space of $99 \times 67 \times 308$ (approximately 2 million cells).

Currents and Fields

Current and SAR distributions have previously been calculated using FDTD in 1.31- and 2.62-cm-resolution models of the human body for frequencies from 20 to 915 MHz [1], and for a 1.31-cm-resolution model at 60 Hz [8]. These 60 Hz calculations demonstrated the usefulness of frequency scaling. Because of the quasi-static nature of the coupling to the human body at 60 Hz and 5 or 10 MHz, this method relies on equating the currents entering the human body due to electric and magnetic fields. The FDTD simulation is run at 10 MHz, and the results are scaled to 60 Hz by multiplying the fields by 60 Hz/10 MHz. For the 1.31-cm-resolution model, one period of the sine wave is 4580 time steps. In [8], the simulation was run for two cycles of the wave, and the peak was found using the peak detection algorithm over the last cycle. In the 6-mm-resolution model, one period of the 10 MHz wave has 10,000 time steps. Since this model is quite large, running even two cycles of the wave is prohibitively expensive. Hence, the two-equation two-unknowns method was developed and used.

The FDTD simulation was run for a frontally incident, vertically polarized electric field of 10 kV/m with an assumed magnetic field of 26.53 A/m (33.33 μT) polarized from arm to arm of the model. Total vertical currents in each layer were calculated, and are shown in Fig. 1. These agree with the analysis of Deno [9]. The dashed line gives the total currents passing through the layer, as would be measured with a loop-type measuring device of the experimental method of Deno. As expected, the currents are passing from head to foot except for some upward-directed currents in the arms. The peak current densities in each layer are shown in Fig. 2. The torso regions have peak values above the recommended 10 mA/m^2 limit [10]. To be certain that these peak currents are not a numerical artifact on the external surface of the body, a detailed examination was made of the layers of the peak current. It was found that these peak currents are, indeed, deep within the body. The one exception is the region containing the arms and hands, which hang at rest at the sides of the body. For these layers, the peak current densities are

roughly in the center of the arm and hand, although large currents were also found in the chest region.

References

1. O. P. Gandhi, et al., *Health Physics* 63 (3), 281-290, 1992.
2. A. Taflove and K. Umashankar, *Proceedings of the IEEE* 77, 682-698, 1989.
3. K. S. Kunz and K. M. Lee, *IEEE Transactions on Electromagnetic Compatibility*, 333-341, 1978.
4. T. Shibata et al., *IEEE Transactions on Microwave Theory and Techniques* 37 (6), 1064-1070, 1988.
5. C. M. Furse et al., submitted to *IEEE Transactions on Antennas and Propagation*, 1995.
6. D. N. Buechler et al., *IEEE Transactions on Microwave Theory and Techniques* 43 (4) 1995.
7. O. P. Gandhi et al., Final Report submitted to the Department of Microwave Research, Walter Reed Army Institute of Research, Washington, DC, 20307-3100, Contract No. DAMD 17-90-M-SA498, August 27, 1990.
8. O. P. Gandhi and J. Y. Chen, *Bioelectromagnetics Supplement 1*, pp. 43-60, 1992.
9. D. W. Deno, *IEEE Transactions on Power Apparatus Systems* 96, 1517-1527, 1977.
10. S. G. Allen et al., *Physica Medica* VII, 77-89, 1991.

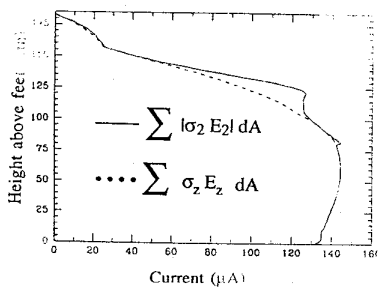

Fig. 1. Total vertical currents passing through the body.

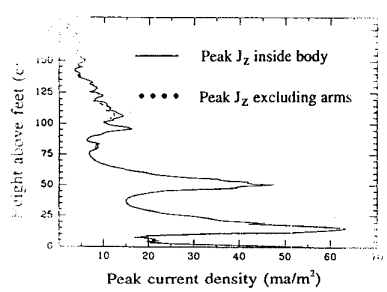

Fig. 2. Peak current density in each layer of the body.